

The Interstellar Dust Properties of Nearby Galaxies

Frédéric Galliano,^{1,2} Maud Galametz,^{1,2} and Anthony P. Jones³

¹IRFU, CEA, Université Paris-Saclay, F-91191 Gif-sur-Yvette, France
email: frederic.galliano@cea.fr, maud.galametz@cea.fr

²Université Paris-Diderot, AIM, Sorbonne Paris Cité, CEA, CNRS, F-91191 Gif-sur-Yvette, France

³Institut d'Astrophysique Spatiale, CNRS, Univ. Paris-Sud, Université Paris-Saclay, Bât. 121, 91405 Orsay, France; email: anthony.jones@ias-u.psud.fr

Xxxx. Xxx. Xxx. Xxx. YYYY. AA:1–41

This article's doi:
10.1146/((please add article doi))

Copyright © YYYY by Annual Reviews.
All rights reserved

Keywords

ISM: dust, Magellanic clouds, nearby galaxies, methods

Abstract

This article gives an overview of the constitution, physical conditions and observables of dust in the interstellar medium of nearby galaxies. We first review the macroscopic, spatial distribution of dust in these objects, and its consequence on our ability to study grain physics. We also discuss the possibility to use dust tracers as diagnostic tools. We then survey our current understanding of the microscopic, intrinsic properties of dust in different environments, derived from different observables: emission, extinction, polarization, depletions, over the whole electromagnetic spectrum. Finally, we summarize the clues of grain evolution, evidenced either on local scales or over cosmic time. We put in perspective the different evolution scenarios. We attempt a comprehensive presentation of the main observational constraints, analysis methods and modelling frameworks of the distinct processes. We do not cover the dust properties of the Milky Way and distant galaxies, nor circumstellar or active galactic nucleus torus dust.

1. INTRODUCTION

1.1. The Interstellar Dust: a Key Galaxy Component

Interstellar grains are solid particles of sizes $0.3 \text{ nm} \lesssim r \lesssim 0.3 \text{ }\mu\text{m}$, made of heavy elements (mainly O, C, Si, Mg, Fe) available in the InterStellar Medium (ISM). They appear to be rather uniformly mixed with the gas. Although accounting for $\lesssim 1\%$ of the ISM mass, they have a radical impact on galaxies, as they scatter and absorb starlight. In normal disk galaxies, they re-radiate in the InfraRed (IR) about 30% of the stellar power, and up to 99% in ultraluminous IR galaxies (*e.g.* Clements et al. 1996). In addition, they are responsible for the heating of the gas in PhotoDissociation Regions (PDR), by photoelectric effect (PE; Draine 1978). They are also catalysts of numerous chemical reactions, including the formation of the most abundant molecule in the Universe, H_2 (Gould & Salpeter 1963).

A detailed knowledge of the grain properties is crucial to study the lifecycle of the ISM and galaxy evolution, as it is needed to: (1) unreddened UV-visible observations; (2) study deeply embedded regions; (3) build reliable diagnostics of the physical conditions and of the evolutionary stage of a galaxy or a star forming region; (4) provide accurate prescriptions in photoionization and photodissociation models, and simulations of the star formation process. However, as we will show in this review, there remains several uncertainties about the grain properties and their evolution. Dust physics is characterized by the great complexity of its object. The number of ways to combine elements to build interstellar solids is virtually limitless and has consequences on the longevity of the particle and its observables. The progress in this field is thus mainly driven by empirical constraints: observations over the whole electromagnetic spectrum (Figure 1); and laboratory experiments on dust analogs.

WHAT ARE THE “DUST PROPERTIES”?

Dust mixture constitution. The constitution of a grain mixture is defined by: (1) the chemical composition of the bulk material and its stoichiometry; (2) the structure of the grains (crystalline, amorphous, porous, aggregated, *etc.*); (3) the presence of heterogeneous inclusions; (4) the presence of organic and/or icy mantles; (5) the shape of the grains; (6) their size distribution; (7) their abundance relative to the gas.

Dust physical conditions. A dust mixture, with a given constitution, can experience different physical conditions: (1) thermal excitation of the grains, due to radiative heating (equilibrium or stochastic), or to collisional heating in a hot plasma; (2) grain charging by exchange of electrons with the gas; (3) alignment of elongated grains on the magnetic field; (4) grain rotation (relevant for the smallest sizes).

Dust observables. A grain mixture undergoing a given set of physical conditions will exhibit the following observables (represented on Figure 1): (1. **Emission**) the emission of a thermal continuum (IR to mm), and molecular and solid state features (Mid-IR; MIR); a possible microwave emission (cm); a possible luminescence (visible); the possible polarization of this emission (IR to mm); (2. **Absorption**) the absorption of the light from a background source by a continuum, as well as molecular and solid state features, including diffuse interstellar bands and ices (X-ray to MIR); the possible polarization of this absorption (UV to visible); (3. **Scattering**) the scattering of the light from a bright source in our direction, and its polarization (X-ray to Near-IR; NIR). (4. **Depletions**) some elemental depletion patterns.

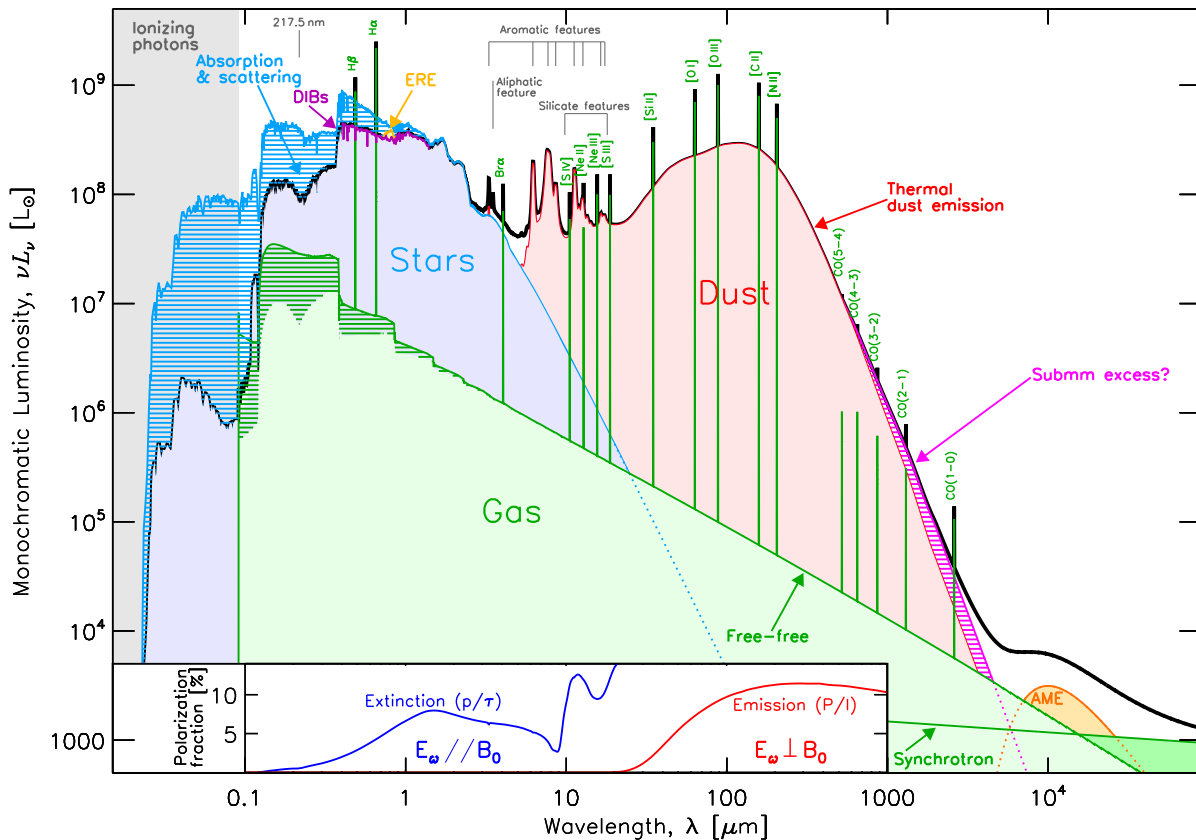


Figure 1

Spectral energy distribution (SED) of a typical late-type galaxy. The blue hatched area shows the power absorbed by dust. We show typical Diffuse Interstellar Band (DIB), Extended Red Emission (ERE) and Anomalous Microwave Emission (AME) spectra, with the most relevant gas lines. The inset shows the model D of Guillet et al. (2017, $G_0 = 100$).

1.2. The Invaluable Laboratories of Nearby Galaxies

Most of our knowledge of the dust properties comes from studies of the Milky Way (MW). However, as it will be demonstrated in this paper, an increasing number of nearby galaxy studies provide unique discriminating constraints on fundamental dust processes. Indeed, nearby galaxies harbor a wider diversity of environmental conditions (metallicity, star formation activity, *etc.*) than what can be found in the MW. In particular, they allow us to observe dust in extreme conditions. Second, they constitute a necessary intermediate step towards understanding distant galaxies, as they are spatially resolved and have a better wavelength coverage. Finally, the interpretation can sometimes be more difficult in the MW, as we see the projected material of its entire disk. On the contrary, high latitude observations of face-on galaxies can provide cleaner sightlines.

We do not have a precise definition of *nearby* galaxies. They constitute a category expanding with the angular resolution of IR observatories. In this review, we consider they are objects closer than $\simeq 100$ Mpc.

Scale-length/height:

the intensity, at radius/azimuth, r , can be written as: $I(r) \propto \exp(-r/l)$, where l is the scale-length/height.

ISO: Infrared Space Observatory ($\lambda \simeq 5 - 210 \mu\text{m}$; 1995 – 1998)

Concentration index: ratio between radii along the major axis encompassing 75 % and 25 % of the total flux of a galaxy.

Spitzer: space telescope ($\lambda \simeq 3 - 160 \mu\text{m}$; 2003 – 2009).

UIB: Unidentified Infrared Bands (cf. Section 3.1.2). Prominent **MIR** features (Figure 1), attributed to carbonaceous grains.

Herschel: space observatory ($\lambda \simeq 55 - 672 \mu\text{m}$; 2009 – 2013).

2. THE MACROSCOPIC DISTRIBUTION OF DUST IN GALAXIES

2.1. The Observational Point of View

2.1.1. The Dust Distribution in Disk Galaxies. Dust biases our understanding of galactic structure, as it affects our derivation of luminosity profiles. The level of dust attenuation can indeed strongly vary depending on the sightline and from one galaxy to another (*e.g.* Calzetti 2001; Pierini et al. 2004; Battisti, Calzetti & Chary 2016). Understanding how dust is distributed in galaxies is a necessary step to correct for these attenuation effects.

2.1.1.1. MIR dust scale-length. *ISO* observations helped assess the **MIR** extent of nearby spirals (especially at 7 and 15 μm). They showed that the **MIR** and optical emission have very similar morphologies and concentration indices (Boselli et al. 2003). However, the **MIR** scale-length tends to be systematically smaller than the optical one (Malhotra et al. 1996) and the arm/inter-arm contrast is larger in the **MIR** than in the optical (Vogler et al. 2005). From a large range of morphologies, Roussel et al. (2001) also found that if the IR-to-optical size ratio does not seem to be affected by the presence of a bar, this ratio is, on the contrary, particularly reduced in H I-deficient galaxies or early-type galaxies (see also Bendo et al. 2002). Numerous analysis have shown that the **MIR** disk has a similar scale-length to that of $^{12}\text{CO}(1-0)$, H α or the radio continuum (Sauvage et al. 1996; Walsh et al. 2002; Vogler et al. 2005). The relation with H α , in particular, indicates that the **MIR** scale-length of a galaxy is determined by its star-forming activity. Indeed, the **MIR** emission is enhanced in star forming regions. With *Spitzer*, the improved sensitivity and spatial resolution opened a new frame to model the distribution of dust inside galaxies and in particular to derive radial profiles. *Spitzer* confirmed that the concentration index varies with wavelength. Studying radial profiles of 75 nearby galaxies, Muñoz-Mateos et al. (2009b) found that the concentration indices drop in the **UIBs** (5.8 and 8.0 μm ; Section 3.1.2). The **MIR** observations at longer wavelengths rather indicate a large variety of behaviours, including galaxies with very intense nuclear, circumnuclear or outer ring emission, thus larger concentration indices (*e.g.* NGC 1291, NGC 1512, NGC 1097, NGC 3351).

2.1.1.2. FIR/submm dust scale-length. From *ISO* observations, it quickly became clear that the disk scale-length of the **IR** emission increases with wavelength (Hippelein et al. 2003), with a Far-**IR** (**FIR**) scale-length larger than the optical scale-length (Tuffs et al. 1996; Alton et al. 1998; Haas et al. 1998; Davies et al. 1999; Trewella et al. 2000). This **FIR** colour gradient observed in the disk suggests that part of the **FIR** emission arises from grains heated by the radially decreasing diffuse InterStellar Radiation Field (**ISRF**). In the edge-on spiral galaxy NGC 891, Popescu & Tuffs (2003) showed that large amounts of **FIR** emission was associated to the extended H I disk, raising the question of whether grains are transported from the inner/optical disk, transferred via interactions or more resistant to destruction by shocks in the outer disk. *Spitzer*, *Herschel*, as well as plane or ground-based **submm** instruments have since then revolutionised our vision of the **FIR/submm** emission and particularly confirm the detection of large cold extended disks (Block et al. 1994; Stevens, Amure & Gear 2005; Hinz et al. 2012). In M 51, the scale-length of the 850 μm underlying exponential disk was estimated as $\simeq 5.5$ kpc (Meijerink et al. 2005). More statistically, Muñoz-Mateos et al. (2009a) and Hunt et al. (2015) examined the exponential dust profiles of 60 – 70 nearby galaxies. They showed that the **FIR** scale-length does not vary strongly with galaxy type and is on average $\simeq 10\%$ larger than stellar scale-lengths.

2.1.1.3. Scale-height Studies. In the Galaxy, a scale-height of the order of 100 pc has been estimated using *IRAS* observations at 100 μm , with a vertical distribution that correlates with the distribution of the H I gas (Boulanger & Perault 1988). Davies et al. (1997) extended the analysis to the colder dust phase using *COBE* data and found a more diffuse 20 K dust component, with a cold dust scale-height of about $\simeq 500$ pc (Davies et al. 1997). Outside our MW, edge-on galaxies are ideal objects to constrain this parameter. Xilouris et al. (1999) studied the stellar and dust disks in five of these edge-on late-type spirals and found that their mean optical-to-dust scale-height ratio was $\simeq 1.8$. This ratio is often used as an *a priori* assumption for disk models (Tempel, Tamm & Tenjes 2010). Quantifying the dust scale-height is undoubtedly more difficult for face-on galaxies. Padoan et al. (2001) proposed a new method to measure the average scale-height in face-on disk galaxies. From the H I data in the Large Magellanic Cloud (LMC), they interpreted the break in the power-law shape of the spectral correlation function as the boundary of the gas mass distribution and velocity field. The method has been since then applied to derive scale-height estimates of the warm and cold dust. In the LMC, Block et al. (2010) found that the break in the power spectrum is occurring on scales of $\simeq 100 - 200$ pc in the FIR. Combes et al. (2012) found similar scale-heights in M 33. The technique is limited by the resolution of the observations: artificial breaks can appear when the scale-height is too close to the resolution scale. Finally, radiative transfer codes are robust tools to model the absorption and re-emission by dust and derive structural parameters (cf. Section 2.2). The model of Baes et al. (2003), for instance, has been used to derive scale-lengths and scale-heights in edge-on galaxies (De Looze et al. 2012a; De Geyter et al. 2015; Viaene et al. 2015). The scale-heights derived in these studies typically range from $\simeq 100$ to 200 pc.

2.1.2. The Dust Distribution in Irregular Galaxies. Irregular galaxies can contain large amounts of atomic gas that typically extend to twice their Holmberg radius (*e.g.* Huchtmeier, Seiradakis & Materne 1981). They are also rich in dust, with very similar optical and MIR scale lengths (Hunter, Elmegreen & Martin 2006). The dust emission in irregular galaxies is clumpy and warm, with a hot dust and UIB emission mostly observed towards bright H II regions. This suggests that massive stars are a major source of heating in these environments (*e.g.* Hunter, Elmegreen & Martin 2006).

2.1.3. The Dust Distribution in Dwarf Galaxies. One of the main characteristics of dwarf galaxies is their low metallicity (Z). As we will see in Section 4.3.2, the dust-to-gas ratio scales roughly with Z . The ISM in these objects is less dusty and thus, more transparent. Similarly to irregular galaxies, massive stars are a major source of heating in these objects (*e.g.* Walter et al. 2007), and they are permeated by SuperNova (SN)-triggered shock waves (*e.g.* Oey 1996). Finally, these galaxies exhibit large H I envelopes. The IR emitting region can correspond to only $\simeq 20 - 30\%$ of the total mass of the system (*e.g.* Walter et al. 2007).

2.1.4. The Dust Distribution in Elliptical Galaxies. Elliptical galaxies possess very little dust: the average dust-to-stellar mass ratio is $\simeq 50$ times lower than that of spiral galaxies (Smith et al. 2012). Dust-lanes are, however, commonly detected in elliptical galaxies (Sadler & Gerhard 1985). Jura et al. (1987) for instance found that half of nearby ellipticals are detected at *IRAS* wavelengths. (Smith et al. 2012) found that the elliptical galaxies detected at 250 μm tend to have higher X-ray luminosities. Their dust may be heated in part by electron collisions (Goudfrooij & de Jong 1995).

IRAS: InfraRed
Astronomical
Satellite
($\lambda = 12 - 100 \mu\text{m}$;
1983).

2.1.5. The Dust Distribution in Galactic Superwinds. Dust at high latitudes or in galactic haloes can be explained as resulting from various mechanisms, among which stellar feedback, transport via cosmic-ray driven winds or radiation pressure on the grains (Bocchio et al. 2016). The latter mechanism could also partly contribute to drive the galactic superwinds in star-forming galaxies even if several studies have shown that it is insufficient to be the only mechanism (Hopkins, Quataert & Murray 2012; Contursi et al. 2013). Contursi et al. (2013) showed that, in the outflow of M 82, dust is slower than the ionized and molecular gas, indicating that dust grains are kinematically decoupled from the gas in the superwind. Most of this dust is not fast enough to escape and may fall back into the galaxy disk.

2.1.6. Dust Heating Sources Probed With Infrared Colours. Dust emits in the IR–submm. In this regime, the ratio of two fluxes (or *colour*) provides information on the grains, the same way optical colours provide information on the stars. These colours are widely used to understand the sources of heating of ISM dust. From *IRAS* observations, Lonsdale Persson & Helou (1987) were among the first ones to use the correlation of the $L_\nu(60)/L_\nu(100)$ colour temperature with tracers of the old stars, to study their heating contribution. With *Spitzer* observations, global $L_\nu(8)/L_\nu(160)$ ratios were then used to probe the origin of the UIBs (cf. Section 3.1.2) and to show that their emission correlates surprisingly well with that of the diffuse, cold dust (e.g. Bendo et al. 2008). Resolved observations later showed that enhancements in the $L_\nu(8)/L_\nu(160)$ ratio are spatially offset relative to the star forming regions, suggesting that the UIBs could be partly excited by photons leaking out of star forming regions (Jones et al. 2015) by up to 30 – 40 % (Crocker et al. 2013).

With the arrival of *Herschel*, the study was pushed towards longer wavelengths, tracing dust at lower temperatures. *Herschel* ratios have been extensively correlated with both stellar surface brightnesses and star formation rate tracers. These analyses usually find a strong correlation of the $L_\nu(250)/L_\nu(350)$ and $L_\nu(350)/L_\nu(500)$ ratios with the local stellar mass, showing the importance of the lower-mass stellar populations as a heating source of the coldest dust population (Bendo et al. 2010; Boquien et al. 2011). By correlating the submm ratios with a linear combination of tracers of the total stellar population (1.6 μm) and of the star forming regions ($\text{H}\alpha$), Bendo et al. (2012) could segregate the two different heating sources and found that $\simeq 60 - 90\%$ of the heating of cold dust is assured by lower-mass stars, in disk galaxies. Ratios at shorter wavelength, such as $L_\nu(70)/L_\nu(160)$ or $L_\nu(160)/L_\nu(250)$, are less correlated with radius and more strongly correlated with the Star Formation Rate (SFR). Boselli et al. (2010) and Boquien et al. (2011) found similar results, showing in particular that the warm dust temperature as measured by the $L_\nu(60)/L_\nu(100)$ ratio seems to increase with the birthrate parameter, b , whereas the cold dust temperature, (measured by the $L_\nu(350)/L_\nu(500)$ ratio) seems to be anti-correlated with b . However, the old stellar population probably continues to also play a role in the heating of the warm dust, with a contribution that seems to correlate with the galaxy evolutionary stage (for instance significant global contribution of the bulge stars in early-type galaxies like M 81; Bendo et al. 2012). On the other hand, Rémy-Ruyer et al. (2013) showed a trend of colour temperature with metallicity, suggesting that low- Z systems are on average hotter (see also Melisse & Israel 1994). This is conjectured to be due to the enhanced contribution of young star heating at low- Z .

New results from radiative transfer models (cf. Section 2.2) are now quantifying better the respective contributions of the different stellar populations to dust heating. In M 31, Viaene et al. (2017) showed that 90 % of the dust could be heated by the lower-mass stellar

Monochromatic luminosity: we note $L_\nu(\lambda)$, the monochromatic luminosity (L_\odot/Hz), at wavelength λ (μm).

Birth rate parameter: current SFR divided by the mean SFR over the lifetime of the galaxy.

populations (see their Fig. 8). Further detailed analysis would be necessary to quantify more robustly the contribution as a function of the galaxy type.

2.2. The Radiative Transfer Approach

WHAT ARE THE SPATIAL SCALES RELEVANT TO DUST HEATING?

The dust physical conditions vary on spatial scales of the order of the mean free path of a *V*-band photon:

$$l_V = \left[\underbrace{\overbrace{Y_{\text{dust}}}^{\text{dust-to-H mass ratio}} \times \overbrace{m_{\text{H}}}^{\text{mass of an H}} \times \overbrace{n_{\text{H}}}^{\text{density}}}_{\text{dust mass per unit ISM volume}} \times \underbrace{\kappa(V)}_{\text{dust opacity}} \right]^{-1} \simeq \frac{600 \text{ pc cm}^{-3}}{n_{\text{H}}}. \quad (1)$$

For a diffuse region ($n_{\text{H}} \simeq 10 \text{ cm}^{-3}$), $l_V \simeq 60 \text{ pc}$, while for a dense region ($n_{\text{H}} \simeq 10^4 \text{ cm}^{-3}$), $l_V \simeq 0.06 \text{ pc}$. Thus, to resolve dust temperature variations, in an edge-on cloud, we would need to resolve structures of $\simeq 0.06 \text{ pc}$, which translates into $\simeq 0.2''$ for the LMC (typical *ALMA* & *JWST* resolution) and $\simeq 0.01''$ in M31 (currently inaccessible). For a face-on cloud, there will be mixing along the line of sight, in any case.

2.2.1. Radiative Transfer Models. The most rigorous way to understand the effects of dust extinction and emission on UV-to-mm observations of galaxies is to model the Radiative Transfer (RT) of the starlight through their dusty ISM, in a realistic 3D geometry. Several teams have developed such codes for disk galaxies (*e.g.* Baes et al. 2003; Bianchi 2008; Popescu et al. 2011). These codes solve the RT equation, accounting for multiple anisotropic scattering, absorption, and dust and stellar emission. This type of computation is numerically intensive. Most models implement a Monte Carlo method, with various refinements and heavy parallelization.

2.2.2. Application to Galaxies. Applying 3D RT models to reproduce the spatial flux distribution of galaxies, in all wavebands, is not straightforward. Indeed, the observations provide only 2D projected constraints. This is why most studies favor edge-on galaxies, as the images of such objects provide constraints on both the radial and azimuthal distributions, assuming axisymmetry (Figure 2). Several studies have modelled the effect of extinction on the optical data of disk galaxies using such codes (*e.g.* Xilouris et al. 1999; Alton et al. 2004; Bianchi 2007). They were able to answer the recurring question about the optical thickness of disk galaxies (Disney, Davies & Phillipps 1989). In particular, Xilouris et al. (1999) found that the face-on optical depth of typical spiral galaxies is less than one in all optical bands. These studies also provide a more comprehensive answer to the nature of the dust heating sources and on the scale-length and scale-height (cf. Sections 2.1.6 and 2.1.1.3). Finally, these models account for the energy balance between the escaping UV-visible light and the re-emitted IR-submm radiation. Interestingly enough, several studies report a deficit of modelled FIR emission by a factor $\simeq 3-4$, compared to the observations (Alton et al. 2000, 2004; Dasyra et al. 2005; De Looze et al. 2012a,b). This discrepancy is thought to reside in a lack of details in modelling the geometry. In particular, the presence

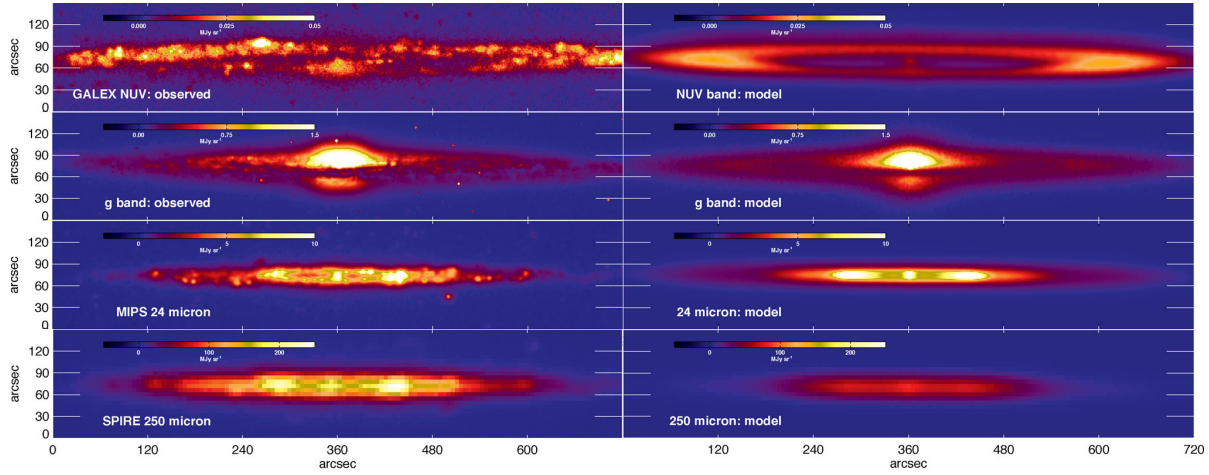


Figure 2

RT model of NGC 4565 (De Looze et al. 2012a). The observations (left column) are compared to the model (right column).

of young stars, deeply embedded in molecular clouds, could compensate this deficit without significantly altering the extinction (e.g. Baes et al. 2010).

2.3. Phenomenological SED Modelling

2.3.1. The Mixing of Physical Conditions. Radiative transfer is impractical in most cases, as the geometry of the source is often poorly known. In addition, radiative transfer models of whole galaxies do not resolve spatial scales small enough (Equation 1). Hence, we are usually compelled to make approximations about the complex topology of the studied object.

2.3.1.1. The Isothermal approximation. To first order, one can ignore the variations of the physical conditions. The Modified Black Body (MBB), the most widely used approximation, assumes that the IR emission comes from identical grains, at a single temperature, T_{dust} , with a power-law, wavelength-dependent, dust mass absorption coefficient, or *opacity*:

$$\underbrace{L_{\nu}(\lambda)}_{\text{monochromatic luminosity}} = \underbrace{M_{\text{dust}}}_{\text{dust mass}} \times \underbrace{\kappa(\lambda_0) \cdot (\lambda_0/\lambda)^{\beta}}_{\text{parametric opacity}} \times \underbrace{4\pi B_{\nu}(\lambda, T_{\text{dust}})}_{\text{black body}}. \quad (2)$$

In principle, a fit of this model, varying M_{dust} , T_{dust} and β , provides constraints both on the grain physical conditions (through T_{dust}), and on their composition (through β). Indeed, different materials can have different β . An inverse $T_{\text{dust}} - \beta$ relation is also observed on some laboratory analogs (e.g. Mennella et al. 1998; Boudet et al. 2005). However, a gradient of temperature tends to broaden the SED. The inherent mixing of physical conditions is thus enough to bias these estimates (e.g. Juvela & Ysard 2012; Hunt et al. 2015). In addition, the contribution from out-of-equilibrium grains can be non negligible at $\lambda \lesssim 70 \mu\text{m}$ (Figure 3-a). In that sense, the MBB derived parameters are ambiguous effective quantities (T_{eff} , β_{eff}), which can be reliably interpreted in terms of intrinsic grain properties only: (1) in diffuse regions, where the ISRF is expected to be roughly uniform, or in cold cores; and (2) provided that the fit is constrained at long enough wavelengths ($\lambda \gtrsim 100 \mu\text{m}$).

ISRF intensity: U is the ISRF intensity, integrated in $[0.0912, 8] \mu\text{m}$. It is normalized so that $U = 1$ in the solar neighborhood.

Alternatively, one can also fit an observed SED, with a full dust mixture (such as in Figure 3-a), varying the ISRF intensity, U , and the mass of each sub-components (Figure 3-b). With such an approach, the MIR wavelengths can be interpreted in terms of size distribution variations, provided that the ISRF is roughly uniform.

DUST HEATING REGIMES: EQUILIBRIUM OR STOCHASTIC?

Thermal Equilibrium. The enthalpy, H , of grains with large enough radii ($r \gtrsim 0.02 \mu\text{m}$) is, in most cases, significantly higher than the mean energy of the incident photons they absorb, $\langle h\nu \rangle \ll H$. Therefore, a single photon event does not notably modify their temperature. They are at equilibrium with the radiation field. Their spectrum is proportional to a Planck function times a wavelength-dependent opacity (Figure 3-a).

Stochastic Heating. On the opposite, for small grains ($r \lesssim 0.02 \mu\text{m}$), $\langle h\nu \rangle \gtrsim H$. A single photon event will cause temperature spikes at a few hundred K (depending on its size), followed by a significant cooling before the next absorption (Draine & Anderson 1985). These temperature fluctuations result in a broad spectrum, extending down to the MIR (Figure 3-a). Such grains are out of thermal equilibrium.

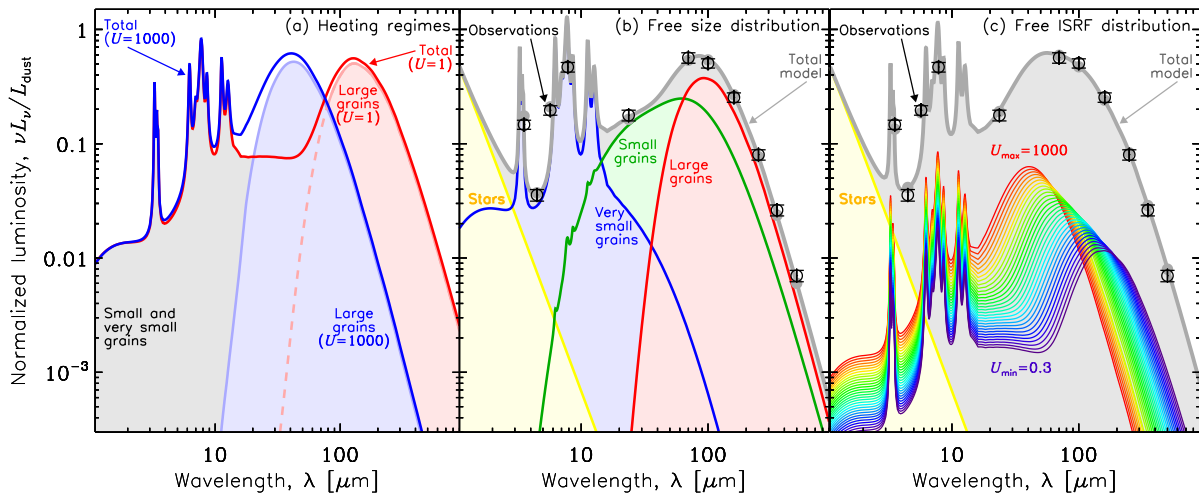


Figure 3

Phenomenological SED modelling. (a) Dust emission model of the MW (J17), heated by the ISRF of the diffuse ISM ($U = 1$; red) and higher ($U = 1000$; blue). It demonstrates that the shape of the SED of small, out-of-equilibrium grains (grey), is independent of U . On the contrary, the shape of the SED of large grains, which are at equilibrium with the ISRF, shifts to shorter wavelengths when U increases, as their equilibrium temperature increases. (b) Simulated broadband observations (black), fitted by varying the mass fractions of *very small* ($0.35 \leq r < 1.5 \text{ nm}$; blue), *small* ($1.5 \leq r < 20 \text{ nm}$; green) and *large* ($0.02 \leq r < 0.3 \mu\text{m}$; red) grains, with a single $U = 8$ (fitted). (c) Same simulated observations as in panel (b), alternatively fitted with a starlight intensity distribution ($\propto U^{-\alpha}$; rainbow curves).

2.3.1.2. Distributions of starlight intensities. It is possible to empirically account for the mixing of physical conditions, by parameterizing the ISRF intensity distribution. One of

the most useful prescriptions is given by Dale et al. (2001). It assumes that the dust mass in different bins of U follows a power-law: $dM_{\text{dust}} \propto U^{-\alpha} dU$ for $U_{\text{min}} < U < U_{\text{max}}$. This way, varying the parameters U_{min} , U_{max} and α , an observed SED can be fit with a combination of physical conditions. This is demonstrated in Figure 3-c. One of the limitations of this approach is that it ignores the variations of the grain properties with environments. As will be discussed in Section 4.2, the carriers of the UIBs are usually destroyed in regions of high U . The FIR emissivity will also change due to mantle processing and evaporation (cf. Section 4.2.1). In addition, there is a degeneracy between the ISRF distribution and the fraction of small grains. This is demonstrated in panels b and c of Figure 3. The same SED is fitted either with an isothermal model, accounting for the MIR fluxes by raising the fraction of small grains (b); or by adding hotter regions (c). Fortunately, the dust mass is dominated by the coldest large grains, and can thus be reasonably derived with this type of model. This type of model is superior to MBB, as the latter underestimates the mass by $\simeq 30\%$ in rather diffuse regions, and down to a factor of $\simeq 3$, where there is a lot of mixing (e.g. Galliano et al. 2011; Galametz et al. 2012; Rémy-Ruyer et al. 2015).

More complex parameterizations of the ISRF distribution are possible (e.g. DL07). It is also possible to build multi-component models, where the phase composition is linked to the star formation history (e.g. da Cunha, Charlot & Elbaz 2008).

2.3.1.3. A Matriochka effect. A consequence of the mixing of physical conditions is that the derived dust mass depends on the spatial resolution. Indeed, cold regions have a weak luminosity, but can be massive. When a large region is integrated, the cold components can be hidden, while they can be accounted for in smaller resolution elements. In practice, the derived dust mass is always higher (up to $\simeq 50\%$), when estimated at high spatial resolution, than on integrated fluxes (Galliano et al. 2011; Galametz et al. 2012; Roman-Duval et al. 2014). The estimate at high resolution is thought to be more accurate. This result depends on the environment, on the maximum resolution and on the parameterization of the ISRF distribution. It is not always seen (e.g. Aniano et al. 2012).

2.3.2. Fitting Methodologies. SED fitting is a technical matter. First, the contribution to the broadband fluxes of several non-dust-related processes, need to be subtracted, or at least accounted for in the uncertainties (Figure 1): (1) the free-free and synchrotron radio continuum; (2) ionic, PDR and molecular lines; (3) foreground Galactic and zodiacal emission; (4) background galaxies. Second, finding the best model parameters is not straightforward. The least-squares method is the most widely used approach to fit an SED model to IR observations. However, Shetty et al. (2009) have shown that this approach leads to a noise-induced false anticorrelation between T_{dust} and β , in the case of a MBB. It makes the determination of the possible real $T_{\text{dust}} - \beta$ relation (Section 2.3.1.1) difficult. Galliano (submitted; hereafter G18) showed that similar noise-induced correlations are found between most parameters, when using full dust models with an ISRF distribution.

Bayesian inference is becoming increasingly popular with the development of powerful computers. Several SED models implement it to provide rigorous uncertainty estimates of the derived parameters. However, G18 has shown that this approach is not sufficient to solve the noise-induced correlations. In fact, Kelly et al. (2012) have demonstrated, in the case of a MBB, that it is necessary to use the more complex *hierarchical Bayesian* inference to achieve this goal. G18 has extended this technique to full dust models with ISRF distributions, and has shown that it leads to significant improvements in the recovery

of the dust parameters and of their intrinsic correlations.

2.4. The Grains in Relation with the Gas and the Stars: Diagnostic Tools

2.4.1. Dust-Related Star Formation Rate Indicators. The SFR is a crucial quantity for galaxy evolution studies. Several dust-related SFR tracers have been empirically calibrated using observations of resolved star forming regions in nearby galaxies. They rely on the fact that young stars are extremely luminous and are enshrouded with dust. If the clouds are optically thick and if their covering factor is unity, the OB star luminosity is: $L_{\text{OB}} \simeq L_{\text{TIR}}$. Contrary to a common misconception, this is independent of dust properties. Assuming a typical Initial Mass Function (IMF), burst age and metallicity, L_{OB} can be converted to: $\text{SFR}/(M_{\odot}/\text{yr}) \simeq 10^{-10} \times L_{\text{TIR}}/L_{\odot}$. The contribution of old stars to L_{TIR} is negligible for high enough SFRs. Alternatively, monochromatic SFR indicators have been proposed. Calzetti et al. (2007) and Li et al. (2010) found that the 24 and 70 μm monochromatic luminosities were good local SFR indicators (on spatial scales of $\simeq 0.5 - 1$ kpc): $\text{SFR}/(M_{\odot}/\text{yr}) \simeq 2611 \times [L_{\nu}(24)/(L_{\odot}/\text{Hz})]^{0.885}$ and $\text{SFR}/(M_{\odot}/\text{yr}) \simeq 1547 \times L_{\nu}(70)/(L_{\odot}/\text{Hz})$. Otherwise, Peeters, Spoon & Tielens (2004) found that, although the 6.2 μm UIB correlates with SFR, it is probably a better B star tracer. Moreover, the UIB strength is strongly metallicity dependent (Section 4.3.4). Finally, several composite indicators have been calibrated (Hao et al. 2011). By combining Far-UV (FUV) or H α measurements with the 24 μm or TIR indicators, they account for the fact that star forming regions are not completely opaque.

TIR: total infrared ($\lambda = 3 - 1000 \mu\text{m}$). L_{TIR} is the integrated power in this range.

2.4.2. Estimating the Total Gas Mass. The complexity of the ISM phase mixing makes the total gas mass difficult to estimate. The ionized, neutral atomic and molecular phases, require each one an independent tracer. And even when these tracers are available, some notable biases question the reliability of these estimates: (1) the [H I]_{21 cm} emission can be saturated at high optical depth, leading to a possible underestimate of $N(\text{H I})$ by a factor up to $\simeq 2$ (e.g. in the local ISM; Fukui et al. 2015); (2) the $^{12}\text{CO}(J=1 \rightarrow 0)_{2.6\text{mm}}$, used to estimate $N(\text{H}_2)$, can be biased by the selective photodissociation of CO in translucent H₂ clouds, leading to a possible underestimate of $N(\text{H}_2)$ by a factor up to $\simeq 100$ (e.g. in low- Z systems; Madden et al. 1997). There is thus a reservoir of *dark gas*, unaccounted for by these tracers. UV H I and H₂ absorption lines are less biased, but are difficult to observe.

Whether observed in extinction or in emission, dust has been used as an indirect gas tracer for several decades (Hildebrand 1983; Devereux & Young 1990). Neglecting the ionized gas, and assuming that the H I surface density, $\Sigma_{\text{H I}}$, has been corrected for optical thickness, the dust surface density can be expressed as: $\Sigma_{\text{dust}} = Z_{\text{dust}} \times (\Sigma_{\text{H I}} + \alpha_{\text{CO}} I_{\text{CO}})$, where α_{CO} is the conversion factor between the CO intensity, I_{CO} , and the H₂ surface density. Israel (1997) pioneered in deriving α_{CO} in nearby galaxies, using the FIR dust emission. Leroy et al. (2011) designed a method to solve both for Z_{dust} and α_{CO} , assuming a homogenous grain constitution and a constant Z_{dust} in each one of the objects they studied. They confirmed that low- Z galaxies have larger α_{CO} than the MW (up to a factor of $\simeq 20$). This well-established fact is believed to originate in the enhanced photodissociation of CO in an ISM less dusty, thus less opaque (cf. Section 4.3.2), while H₂ remains self-shielded. Similar studies have been done in extinction (e.g. in the LMC; Dobashi et al. 2008).

Dust-to-gas mass ratio: noted Z_{dust} , defined as $Z_{\text{dust}} = \Sigma_{\text{dust}}/\Sigma_{\text{gas}}$, where Σ_{gas} is the total gas mass surface density (H II, H I and H₂, including He).

2.4.3. Constraints for Photodissociation Models. In PDRs, the gas is primarily heated by photoelectrons ejected from the grains (Draine 1978). The PE heating is more efficient for the smallest sizes, in particular, for the carriers of the UIBs (e.g. Weingartner & Draine 2001). This heating efficiency therefore depends on the dust properties, and thus on the environment. Assuming that $[\text{C II}]_{158\mu\text{m}}$ is the main gas coolant, the PE efficiency, ϵ_{PE} , can be approximated by the gas-to-dust cooling ratio: $\epsilon_{\text{PE}} \simeq L_{\text{C II}}/L_{\text{TIR}}$. Detailed studies usually add other lines to the gas cooling rate, like $[\text{O I}]_{63\mu\text{m}}$, to have a more complete estimate (e.g. Cormier et al. 2015). Overall, Smith et al. (2017) found that $0.1\% \lesssim \epsilon_{\text{PE}} \lesssim 1\%$, with an average of $\langle \epsilon_{\text{PE}} \rangle \simeq 0.5\%$, in a sample of 54 nearby galaxies. It appears that ϵ_{PE} is lower when the dust temperature is higher (Rubin et al. 2009; Croxall et al. 2012). This is not likely the result of the destruction of the UIB carriers, as their intensity correlates the best with the $[\text{C II}]_{158\mu\text{m}}$ emission (e.g. Helou et al. 2001). It is rather conjectured to be due to the saturation of grain charging in UV-bright regions. The shape of the ISRF also has a consequence on the accuracy with which L_{TIR} represents the true UV, PE-efficient flux. Indeed, Kapala et al. (2017) showed that the variations of ϵ_{PE} in M 31 could be explained by the contribution of old stars to L_{TIR} . Finally, one of the most puzzling features is that ϵ_{PE} is higher at low metallicity (Poglitsch et al. 1995; Madden et al. 1997; Cormier et al. 2015; Smith et al. 2017), while the UIB strength drops in these systems (Section 4.3.4). This is currently poorly understood. However, in the extreme case of I Zw 18 ($Z \simeq 1/35 Z_{\odot}$), where no UIB is detected and the PE heating is estimated to be negligible, the gas-cooling-to-TIR ratio is still $\simeq 1\%$ (Lebouteiller et al. 2017). In this instance, the gas could be heated by X-rays.

Now, studies focusing on the gas properties usually run PDR models with build-in PE-efficiency (e.g. Le Petit et al. 2006). In this case, dust parameters such as L_{TIR} , the visual attenuation or the UIB strength help refine the gas modelling (e.g. Chevance et al. 2016).

3. CONSTRAINTS ON THE MICROSCOPIC DUST PROPERTIES

3.1. The Infrared Emission

3.1.1. Constraints on the FIR Grain Opacity. The dust mass and excitation derived from fits of the SED depend directly on the assumed grain opacity. To first order, it can be approximated by a power-law, in the FIR/submm (Figure 4a). Most studies assume a fixed absolute opacity, $\kappa(\lambda_0)$, and explore the variations of the emissivity index, β .

Table 1 Free emissivity index MBB fits of nearby galaxies by the *Planck* collaboration.

	Milky Way	M 31	LMC	SMC
T_{eff}	19.7 ± 1.4 K	18.2 ± 1.0 K	21.0 ± 1.9 K	22.3 ± 2.3 K
β_{eff}	1.62 ± 0.10	1.62 ± 0.11	1.48 ± 0.25	1.21 ± 0.27
Reference	<i>Planck</i> (2014)	<i>Planck</i> (2015b)	<i>Planck</i> (2011a)	<i>Planck</i> (2011a)

3.1.1.1. Studies of the emissivity index. There are numerous publications presenting MBB fits of nearby galaxies. However, as discussed in Section 2.3.1, the derived β_{eff} is degenerate with temperature mixing. The best constraints on the intrinsic β are obtained in the submm regime, where only massive amounts of very cold dust ($T \lesssim 10$ K) could bias the value. Table 1 lists β_{eff} for several objects, obtained with *Planck*, with constraints up to $850 \mu\text{m}$. It appears that all the values are lower than 2, and that low- Z systems have

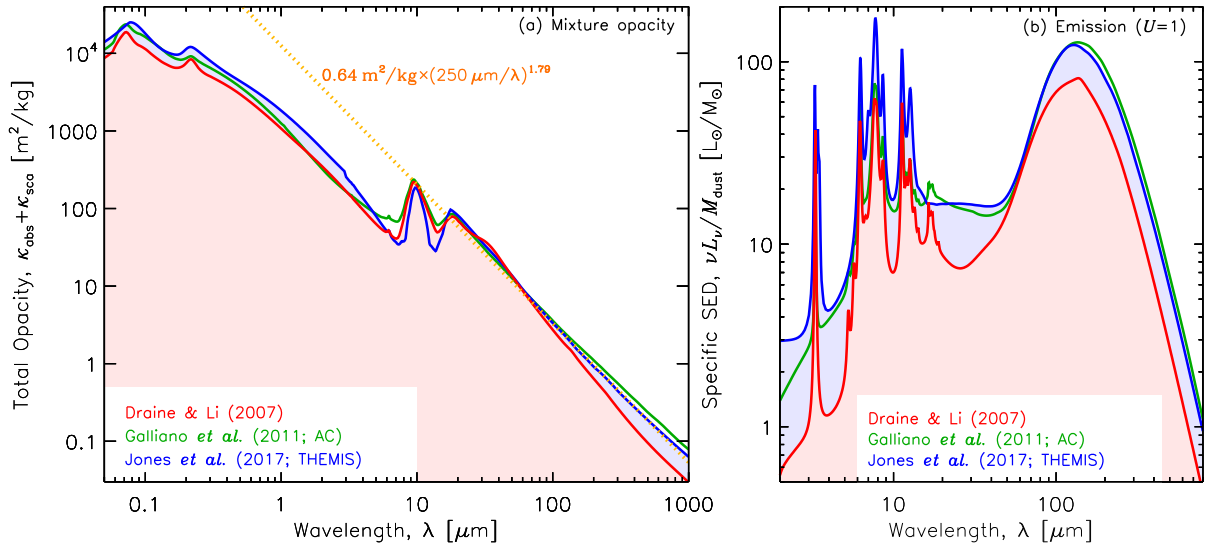


Figure 4

Emissivity of select dust models. (a) Extinction opacities. Notice the different submm slopes. A power-law approximation to J17 is shown in dashed yellow ($\beta = 1.79$, $\lambda_0 = 250 \mu\text{m}$, $\kappa(\lambda_0) = 0.64 \text{ m}^2 \text{ kg}^{-1}$). (b) Corresponding emissivities.

a lower β_{eff} than higher Z galaxies. Boselli et al. (2012) studying a volume-limited sample with *Herschel* (up to $500 \mu\text{m}$) also found an average $\beta_{\text{eff}} \simeq 1.5$, and hinted that low- Z objects tends to have $\beta_{\text{eff}} < 1.5$. In M33, β_{eff} derived from *Herschel* observations is around 2 in the center and decreases down to 1.3 in the outer parts (Tabatabaei et al. 2014). On the other hand, the outer regions of M31 exhibit a steeper slope ($\beta_{\text{eff}} \simeq 2.3$) than in its center (Draine et al. 2014). This contradictory behaviour does not appear to originate in fit biases, as both increasing and decreasing trends of β_{eff} with radius are found in the sample of Hunt et al. (2015).

3.1.1.2. Constraints on the absolute opacity. The absolute opacity, $\kappa(\lambda_0)$, is totally degenerate with M_{dust} (Equation 2). The only way to constrain this quantity is to have an independent estimate of M_{dust} . For instance, Galliano et al. (2011) modelled the IR emission of a strip covering 1/4 of the LMC, using optical properties similar to Draine & Li (2007, hereafter DL07). The resulting dust-to-gas mass ratio was higher than the maximum number of elements that could be locked-up in grains. It led them to propose a more emissive mixture (Figure 4) that could solve this inconsistency. The constraint on the elemental depletions was thus used to show $\kappa(\lambda_0)$ should be a factor of $\simeq 2 - 3$ higher. Quite similarly, Planck Collaboration et al. (2016) modelled the all sky dust emission using the DL07 model. However, the A_V estimated along the sightlines of $\gtrsim 200\,000$ quasars was systematically lower than their dust-emission-derived A_V . Their comparison of emission and extinction thus indicates that the Galactic opacity should also be a factor of $\simeq 2$ higher. Finally, in M31, Dalcanton et al. (2015) derived a high spatial resolution map of A_V . As in the Galaxy, the emission-derived A_V map (Draine et al. 2014) is found to be a factor of $\simeq 2.5$ higher. We emphasize that, although each of these studies found evidence of local variations of the emissivity as a function of the density (cf. Section 4.2.1), the

Planck: FIR–cm space telescope ($\lambda \simeq 300 \mu\text{m} - 1 \text{ cm}$; 2009 – 2013).

overall opacity seems to be scaled up compared to DL07. There is growing evidence that the dust opacities might be, in general, more emissive than standard uncoated compact silicate-graphite mixtures.

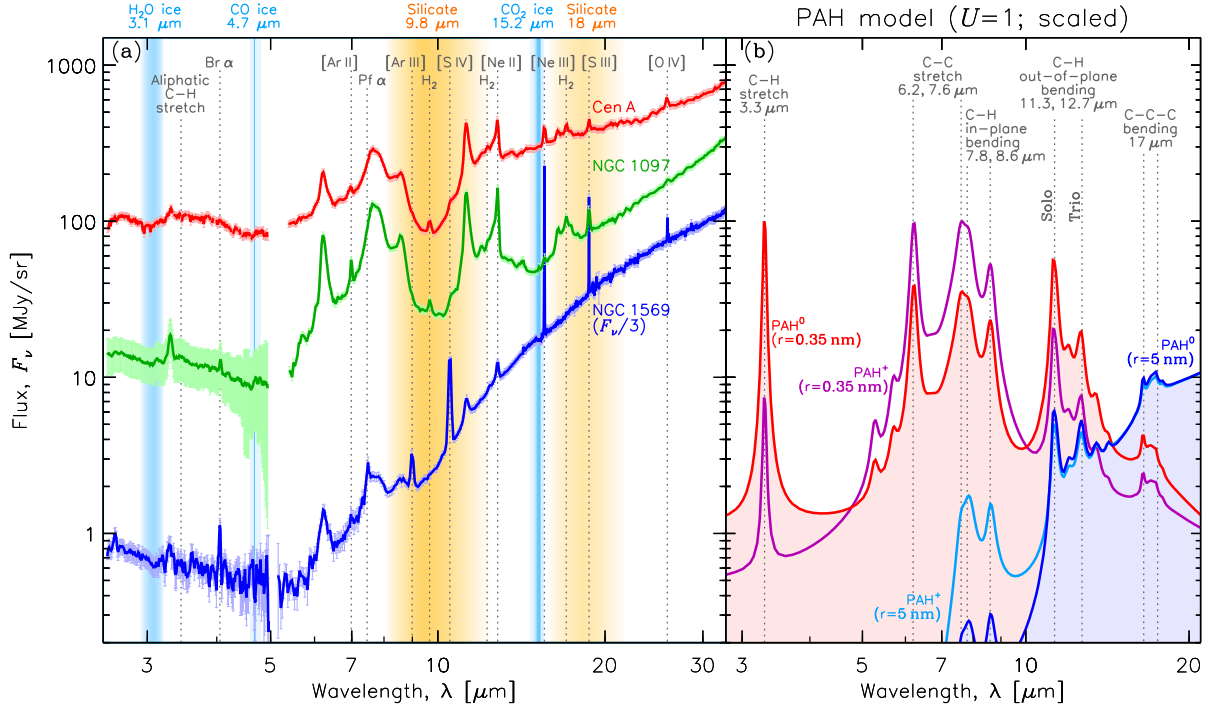


Figure 5

MIR spectra. (a) *AKARI* (2.5 – 5 μm) and *Spitzer* (5 – 30 μm) spectra of the central regions of three galaxies (T. Roland & R. Wu, *priv. comm.*). Cen A is an early-type galaxy with an AGN; it shows strong silicate absorption. NGC 1097 is a late-type starburst with a weak AGN. NGC 1569 is a blue compact dwarf, exhibiting weak AFs and strong ionic lines. (b) Theoretical emission of ionized and neutral PAHs (DL07), with radii r , heated by the diffuse Galactic ISRF ($U = 1$). These spectra are scaled by an arbitrary factor. Solo, trio: one or three C–H bonds on a given aromatic cycle.

Akari: space telescope ($\lambda \simeq 1.7 - 180 \mu\text{m}$; 2006 – 2011).

3.1.2. The Aromatic Feature Spectrum. The MIR range exhibits a complex spectrum of ubiquitous emission bands, that were originally labeled as UIBs (Figure 5). These bands are found in almost every environment. They were first detected in Galactic planetary nebulae (Gillett, Forrest & Merrill 1973). Their relative intensity appeared independent of position in reflection nebulae, leading to the conclusion that they were carried by very small, stochastically heated particles (Sellgren 1984).

3.1.2.1. Candidate materials. It is consensual, nowadays, that the UIBs arise from the vibrational spectrum of a collection of aromatic bonds in a hydrocarbon matrix (the weak 3.4 μm feature is attributed to aliphatic bonds; Duley & Williams 1981). PAHs were proposed by Léger & Puget (1984) and Allamandola, Tielens & Barker (1985). The UIBs likely arise from a statistical mixing of PAHs of different sizes and structure, averaging out drastic variations of the band profiles. Most studies interpret their MIR spectra, in light

of this class of molecules. The main physical processes controlling the shape of the PAH spectrum are the following.

Charge. PAH⁺ have brighter 6 – 9 μm features than PAH⁰, and inversely for the other bands (Figure 5-b). Select band ratios, such as $L_{7.7}/L_{11.3}$, increase with the charge.

Size distribution. Small PAHs fluctuate up to temperatures higher than the large ones. Short wavelength bands are therefore more pumped in small PAHs, while large PAHs emit predominantly long wavelength features (Figure 5-b).

ISRF hardness. The hardness of the ISRF has an effect similar to the size, as a higher mean photon energy causes the grain to fluctuate up to higher temperatures (*e.g.* Galliano et al. 2008, hereafter G08b).

Molecular structure. C–H out-of-plane bending modes have different frequencies, depending on the number of H atom per aromatic cycle. The 11.3 μm band corresponds to a solo H, found on straight molecular edges, while the 12.7 μm one corresponds to a trio, found on corners of the molecules (Figure 5-b). The solo/trio $L_{11.3}/L_{12.7}$ ratio is thus an indicator of PAH compactness (*e.g.* Hony et al. 2001).

Foreground extinction. The wings of the silicate absorption feature at 9.8 μm selectively extinct more the 8.6 and 11.3 μm band than the other features (Figure 5-a).

Dehydrogenation. It has a similar effect to ionization. However, for PAHs larger than $N_C \simeq 25$, hydrogenation through reactions with abundant atomic H is more important than H loss through unimolecular dissociation (*e.g.* Hony et al. 2001). Thus, dehydrogenation does not have a detectable effect on the UIB spectrum.

However, a mix of fully aromatic and/or partially hydrogenated molecules does not appear to give a completely satisfactory fit to the wavelength position and shape of the observed interstellar emission bands in the 3.3 – 3.5 μm region (*e.g.*, Fig. 3 in Sandford, Bernstein & Materese 2013). Alternatively, the J17 model a-C(:H) nanoparticles could provide a physically-viable alternative to the interstellar PAH hypothesis for the carriers of the UIBs. To date, the J17 interstellar dust model appears to be the only one that is consistent with the presence of the emission bands at $\simeq 3.3$ and $\simeq 3.4$ μm and the associated sub-bands at $\simeq 3.5$ μm. In this model, these bands are due to a-C(:H) nano-grains, of mixed aromatic, olefinic and aliphatic composition, with size-dependent optical properties (Jones et al. 2013). Further, and within the framework of J17, variations in the band ratios in the 3.3 – 3.5 μm region can be explained by a-C(:H) compositional variations as the dust evolves in response to its environment. That is the reason why we adopt the generic acronym UIB. We refer to PAHs only when discussing results depending on the PAH hypothesis.

3.1.2.2. MIR spectrum fitting challenges. To study the properties of the UIBs, one needs to estimate the intensity of each band. Most studies perform least-squares spectral decompositions, with the linear combination of several components (*e.g.* Smith et al. 2007, hereafter S07; G08b): (1) PAHs: Lorentz or Drude profiles; (2) gas lines: Gauss profiles; (3) dust continuum: several MBBs; (4) a stellar continuum. In addition, (5) the extinction by silicate and ices can be parameterized by their optical depths. However, as can be seen on Figure 5-a, the wings of the UIBs can be difficult to distinguish from the dust continuum. In addition, several features are blended (*e.g.* the 6 – 9 or 17 μm complexes) and may present underlying broad plateaus. These bands can also be blended with ionic lines, at low spectral resolution (*e.g.* the 12.7 μm and [Ne II]_{12.81μm}). This type of fit can thus lead to some biases and degeneracies in the following cases (G08b): (1) low signal-to-noise ratio;

PAH: polycyclic aromatic hydrocarbons. Molecules composed of several aromatic cycles, with peripheral H atoms.

a-C(:H): amorphous carbon with partial hydrogenation. Solids containing both aromatic and aliphatic bonds, in proportion depending on the H-fraction.

(2) low **UIB**-to-continuum ratio; (3) moderate extinction. The derived band intensities are also sensitive to the adopted **UIB** positions and widths, and on the nature and number of **MBB** components for the continuum.

3.1.2.3. Aromatic band ratios in nearby galaxies. G08b studied the 6.2, 7.7, 8.6 and 11.3 μm **UIBs**, in a sample of nearby galaxies and Galactic regions. Several band ratios were used in order to solve the degeneracies between the effects of the charge, size distribution, **ISRF** hardness and extinction. The $L_{6.2}/L_{11.3}$ and $L_{7.7}/L_{11.3}$ ratios vary by a factor of $\simeq 10$. Among this sample, covering a large range of physical conditions and spatial resolutions, it appears that most of the variations of the band ratios arise from variations of the **PAH** charge. S07 also found large variations of the band ratios (by a factor of $\simeq 2 - 5$) in central regions of starbursts and **AGNs**. However, they found that the presence of a low-luminosity **AGN** could alter the spectrum, by destroying the smallest **PAHs** (also confirmed by Sales, Pastoriza & Riffel 2010). Harsh environments result in selective destruction of the smallest **PAHs**, like in elliptical galaxies (Kaneda, Onaka & Sakon 2007; Vega et al. 2010), or in the superwind of M82 (Beirão et al. 2015).

In low-metallicity systems, the variations can be more difficult to probe, as the band equivalent widths are lower (Figure 5-a; this point is discussed in Sections 4.2.3.1 and 4.3.4). In the **LMC**, Mori et al. (2012) found different trends in neutral and ionized sightlines. Toward the latter, there are evidences that **PAHs** have a lower charge, as a consequence of the higher recombination rate, and are on average larger, due to the destruction of the smallest ones. In contrast, in the **SMC**, Sandstrom et al. (2012) found very weak $L_{6-9}/L_{11.3}$ ratios and weak 8.6 and 17 μm bands, implying small weakly ionized **PAHs**. This last point is consistent with the trend of $L_{17}/L_{11.3}$ with Z found by S07. However, Hunt et al. (2010) argued that Blue Compact Dwarf galaxies (**BCD**) exhibit a deficit of small **PAHs**. If there is a smooth variation of **PAH** size distribution with Z , these results are in contradiction. Sandstrom et al. (2012) noted that these **BCDs** are more extreme environments than the **SMC**, and that photodestruction could dominate the **PAH** processing (cf. Section 4.2.3.1). We note that the solution to this apparent controversy might alternatively reside in the difference in studied spatial scales. In the Magellanic Clouds, *Spitzer* spectroscopy gives a spatial resolution of a few parsecs, compared to a few hundreds in nearby **BCDs**. The fact is that the **LMC** and **SMC** exhibit strong spatial variations of their **UIB** spectrum. Whelan et al. (2013) showed a diversity of **MIR** spectral properties in the **SMC**. They demonstrated that the **PAH** emission in a region like N66 is dominated by its diffuse component, and not by its bright clumps, where **PAHs** are destroyed. At the other extreme, the molecular cloud SMC-B1#1 shows unusually high **UIB** equivalent widths (Reach et al. 2000). Also, the $L_{11.3}/L_{12.7}$ ratio indicates that **PAHs** are more compact in 30 Dor and more irregular outside (Vermeij et al. 2002). All these elements suggest that there is a complex balance of processes shaping the **MIR** spectra throughout low- Z environments.

Finally, **UIB** ratios can be used as a diagnostic tool of the physical conditions. For instance, G08b provided an empirical calibration of the $L_{6.2}/L_{11.3}$ ratio with the **UV**-field-to-electron-density ratio, G_0/n_e (Section 2.4.3). However, the dynamics of the **UIB** ratios being at most a factor of $\simeq 10$, with typical uncertainties of 20%, their diagnostic potential is practically limited to a low/high value dichotomy.

3.1.3. Silicate Features in Emission. Silicates are one of the most abundant dust species ($\simeq 2/3$ of the mass; DL07; J17). They are characterized by two prominent features at 9.8

and 18 μm , corresponding to Si–O stretching and O–Si–O bending modes, respectively (Figure 5-a). These features are most often seen in extinction (Section 3.2.4). They can be seen in emission in galaxies, when the dust is hot enough ($T \gtrsim 150\text{ K}$). It is the case near the central engine of AGNs (Wu et al. 2009; Hony et al. 2011), even low-luminosity AGNs, like the nucleus of M 31 (Hemachandra et al. 2015). The MIR spectra of early-type galaxies also show clear silicate emission features, but likely of circumstellar origin (e.g. Bressan et al. 2006). Alternatively, some dust models present a significant out-of-equilibrium emission from small silicates (e.g. Zubko, Dwek & Arendt 2004). Such small silicates are not unlikely (e.g. Section 3.5.6). In the diffuse ISM, the 9.8 μm feature would be hidden by the bright aromatic features. However, we should be able to see it when the UIB intensity decreases, like in dwarf galaxies. It is usually not the case (e.g. Rémy-Ruyer et al. 2015). It might suggest that either these small silicates have not abundantly formed, or that they are efficiently destroyed in dwarf galaxies.

3.1.4. Aliphatic Feature in Emission. The 3.4 μm aliphatic emission feature is carried by small a-C(:H). The $L_{3.4}/L_{3.3}$ aliphatic-to-aromatic ratio shows regional variations in the ISM, as the result of structural changes in the hydrocarbons through UV processing (e.g. Jones et al. 2013). Yamagishi et al. (2012) detected this feature in the superwind of M 82. They found that the $L_{3.4}/L_{3.3}$ ratio increases with distance from the center. They interpreted this trend as the production of small a-C(:H), by shattering of larger grains in this harsh halo. Similarly, Kondo et al. (2012) found a higher $L_{3.4}/L_{3.3}$ ratio in the nuclear bar of NGC 1097, suggesting that the gas flow towards the center could lead to the formation of small a-C(:H) by shattering. We note that, alternatively, the $L_{3.4}/L_{3.3}$ ratio can increase with the accretion of a-C(:H) mantles in denser regions (Jones et al. 2013). This feature can also be seen in extinction, in AGNs (e.g. Mason et al. 2007).

3.2. The Wavelength-Dependent Extinction

3.2.1. General features. The extinction is the combination of light absorption and scattering. Early dust studies, before IRAS, were mainly based on extinction. In the MW, Cardelli, Clayton & Mathis (1989, C89) demonstrated that the UV-to-NIR extinction curves follow a universal law, parameterized by R_V :

$$R_V \equiv \frac{A_V}{A_B - A_V} \quad \text{with} \quad A_\lambda = 1.086 \times \underbrace{(\kappa_{\text{abs}}(\lambda) + \kappa_{\text{sca}}(\lambda))}_{\text{optical depth, } \tau(\lambda)} \times \underbrace{\Sigma_{\text{dust}}}_{\text{mass surface density}}. \quad (3)$$

The sum of the absorption and scattering opacities, $\kappa_{\text{abs}} + \kappa_{\text{sca}}$, depends on the dust constitution. Such an extinction curve presents different regimes (Figure 6-a): (1) a FUV rise, mainly due to absorption by small grains (Rayleigh limit: $A_\lambda \propto 1/\lambda$); (2) a 217.5 nm absorption bump, probably carried by small carbon grains (PAHs, graphite, amorphous carbon, etc.); (3) an optical knee, mainly due to scattering by large grains; (4) a power-law NIR continuum. On average, $R_V \simeq 3.1$ in the Galaxy, with large variations between sightlines ($R_V \simeq 2 - 5$) due to dust processing, low values of R_V being attributed to regions with enhanced small grains. For a given R_V , the quantity $A_V/N(\text{H})$ is proportional to the dust-to-gas mass ratio.

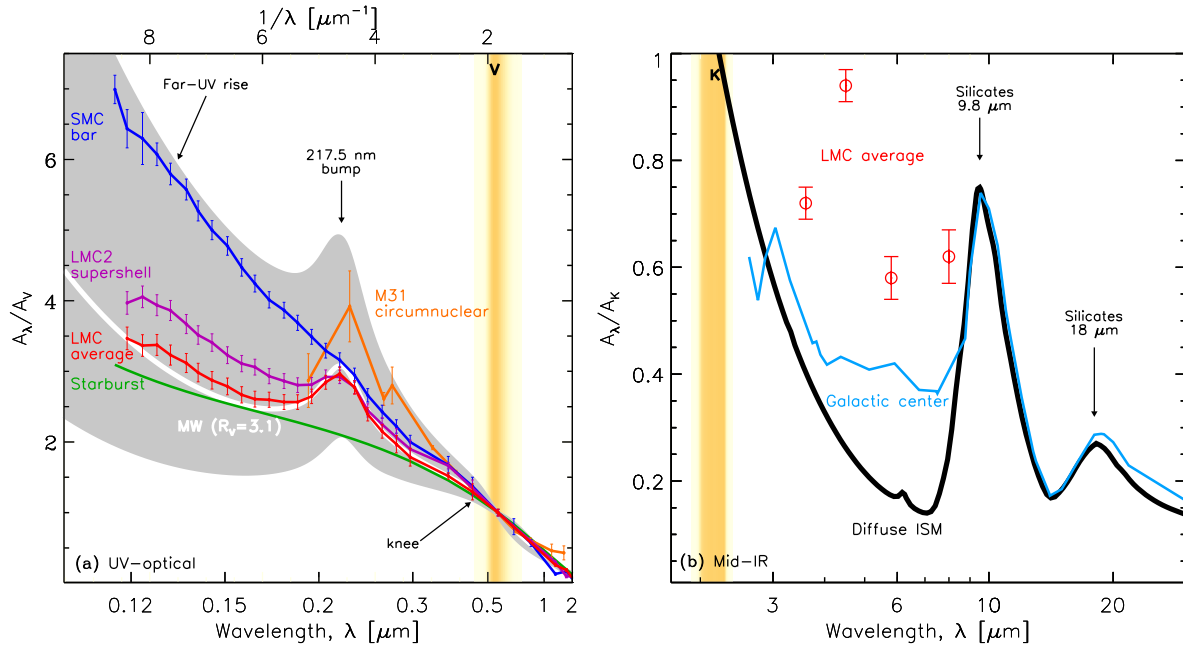


Figure 6

Extinction curves. (a) Extinction curves of the Magellanic clouds (Gordon et al. 2003), compared to the MW (the grey area spans $R_V = 2 - 5$; the white curve corresponds to $R_V = 3.1$ Fitzpatrick 1999). We have also displayed the attenuation curve of starburst galaxies (Calzetti et al. 2000) and of the circumnuclear region of M31 (Dong et al. 2014). (b) MIR LMC average (Gao et al. 2013), compared to the Galactic center (Lutz et al. 1996).

3.2.2. Methodology. The most reliable wavelength-dependent extinction curves are derived using the *pair method* (Stecher 1965). Two stars of the same spectral type are observed, one with a low and one with a high foreground extinction. The extinction curve is directly derived from the differential spectrum, assuming the dust properties are uniform along the two sightlines. In external galaxies, this method has been successfully applied only to the Magellanic clouds (*e.g.* Nandy et al. 1981; Gordon et al. 2003) and M31 (Bianchi et al. 1996; Clayton et al. 2015). Alternatively, a stellar atmosphere model can be used in lieu of the reference star (*e.g.* Fitzpatrick & Massa 2005).

In more distant objects, where observations of individual stars become impractical, other methods, less direct and more model dependent, have to be used. Stellar SED modelling with dust attenuation is widely used (*e.g.* Hutton, Ferreras & Yershov 2015). Attenuation, which is the net loss of photons within a galaxy, differs from extinction because it includes the effects of geometry. There is a degeneracy between dust attenuation and stellar age and metallicity. This degeneracy can be solved by accounting for FIR emission (Gordon et al. 2000) or by studying disks with different inclinations (Conroy, Schiminovich & Blanton 2010, hereafter C10). Alternatively, the ratio of Hydrogen recombination lines can be used. Calzetti, Kinney & Storchi-Bergmann (1994, hereafter C94) derived an average attenuation law (Figure 6-a) using this method, on a sample of 39 starbursts, assuming that all these objects had the same metallicity, stellar populations and dust properties. This average curve is rather flat and has no bump (Figure 6-a). In contrast, C10 derived an average

attenuation law for disk galaxies, based on the UV-visible photometry. They found that the C94 law does not provide a good fit to their curve but that there might be a bump. They point out that it is possible that previous studies failed to recognize the presence of the UV bump, because they tried MW laws only with $R_V = 3.1$.

Finally, other less common methods are available. In a few rare cases, a background lenticular galaxy can be used to probe the extinction in a foreground galaxy (*e.g.* White & Keel 1992; Berlind et al. 1997). Color magnitude diagrams can be used to probe the visible-NIR extinction curves, like the red giant clump (Gao et al. 2013; De Marchi & Panagia 2014). Supernova also provide bright sources probing the extinction in the host galaxy (*e.g.* Patat et al. 2015).

3.2.3. Extragalactic Results. External galaxies help us probe the extinction curves in extreme conditions, beyond the simple R_V parameterization. There is a continuous variation in shape of the extinction curves from the Galaxy to the SMC (Figure 6-a; Gordon et al. 2003). The SMC bar is characterized by a very steep curve ($R_V = 2.74 \pm 0.13$), without 217.5 nm bump. This is the sign of smaller grain size and reduced fraction of carbon, likely the result of grain shattering by supernova shock waves (Clayton et al. 2003; Cartledge et al. 2005). A weak bump is seen in the SMC wing, which is more quiescent. The LMC is intermediate between the Galaxy and the SMC, although there are important variations within. The LMC2 supershell, near the massive star forming region 30 Dor, has a steeper law than the Galaxy ($R_V = 2.76 \pm 0.09$), with a weaker bump. The average LMC is closer to the Galaxy ($R_V = 3.41 \pm 0.28$). Neither the SMC, nor the LMC2 supershell conform to the C89 parameterization. There still remain some uncertainties on these properties. De Marchi & Panagia (2014) studied the visible-NIR curve in 30 Dor, using the spread of the red giant clump in the colour-magnitude diagram, and found a flatter extinction ($R_V \simeq 4.5$) that they attributed to freshly injected large grains.

The extinction curves of M31 ($Z = 1 - 1.5 Z_\odot$) are consistent with the MW (Clayton et al. 2015, pair method). In its circumnuclear region, the curves appear steeper ($R_V \simeq 2.5$), but similar to the Galactic bulge (Dong et al. 2014, SED). In one of the regions studied by Dong et al. (2014), there is a significantly stronger UV bump (Figure 6-a). In contrast, the spiral galaxy M101 appears to have a smaller bump, with a similar continuum (Rosa & Benvenuti 1994, SED). In the edge-on starburst, M82, Hutton, Ferreras & Yershov (2015, SED) find that both R_V and the bump strength decrease outward, with galactocentric distance. The spiral galaxies studied with the overlap method all exhibit MW curves (*e.g.* Dewangan, Singh & Bhat 1999; Deshmukh et al. 2013), as well as early-type galaxies (*e.g.* Goudfrooij et al. 1994; Finkelman et al. 2010). Some AGNs show signs of dust processing, with an absence of features (Crenshaw et al. 2001; Maiolino et al. 2001).

The extinction estimated towards SN II exhibit steep extinction curves ($R_V \simeq 1.5$), probably due to dust shattering by the shock wave (Hill et al. 1995; Amanullah et al. 2014; Hutton, Ferreras & Yershov 2015). The trend is the same towards SN Ia, with more dispersed values ($R_V \simeq 1.2 - 3$; Elias-Rosa et al. 2006; Huang et al. 2017).

3.2.4. Silicate Features in Absorption. In the MIR, the extinction curve is dominated by the two prominent silicate features at 9.8 and 18 μm (Section 3.1.3; Figure 6-b). In the Galaxy, $A_V/A_{9.8\mu\text{m}} \simeq 12$. These absorption features can be seen when sufficient amount of material is obscuring a bright MIR source (like a star forming region or an AGN). They are even seen at extremely low-metallicity (like in SBS 0335-052; $Z \simeq 1/35 Z_\odot$; Thuan, Sauvage

& Madden 1999; Houck et al. 2004). One issue is the composition of these silicates. It is well established that silicates are partially crystalline in circumstellar environments and become completely amorphous in the ISM (e.g. Kemper, Vriend & Tielens 2004). The crystalline-to-amorphous ratio provides clues of dust processing, as crystallization and annealing have high energy barriers. For instance, Spoon et al. (2006) detected distinctive crystalline silicate absorption features in several ULIRGs. Their crystalline-to-amorphous fraction is $\simeq 10\%$. They interpreted this value as the result of fresh injection of crystalline material by the massive star formation. On average, observations of nearby galaxies find mostly amorphous silicates. In a large sample of LIRGs and ULIRGs, Stierwalt et al. (2014) reported the detection of crystalline silicate absorption features in only 6% of their sample, in the most obscure sources.

3.2.5. Ice Absorption Features. In shielded regions, some molecules can freeze out to form icy grain mantles. The dominant species, H₂O, CO and CO₂ produce MIR absorption bands (Figure 5-a). In the Magellanic clouds, ice absorption can be studied in individual young stellar objects (e.g. Oliveira et al. 2013). In other galaxies, ice features likely come from molecular clouds. ULIRGs show particularly high ice optical depths, correlated with the silicates (Stierwalt et al. 2014). However, some galaxies with high silicate absorption do not present detectable ice features, suggesting that the density of the medium is not the only parameter; the presence of an AGN could prevent ice formation. In nearby star forming galaxies, Yamagishi et al. (2015) conducted an extensive analysis of the CO₂-to-H₂O ice absorption ratio. This ratio exhibits variations by a factor $\simeq 20$, as H₂O has a longer lifetime (higher sublimation temperature) than CO₂. They found this ice ratio correlates best with specific SFR (sSFR), indicating a high ratio in young star forming galaxies.

3.3. Elemental Depletion Patterns

3.3.1. Definition & Method. Dust is made of the available heavy elements produced by stars. In the ISM, a fraction of these elements is in the gas and the rest is locked up into dust. The fraction of missing elements from the gas is called *depletion*. In the MW, where depletions have been studied for most relevant heavy elements, in several hundreds of sightlines through the diffuse neutral medium (Jenkins 2009), it appears that: (1) *refractory* elements, the elements with a higher condensation temperature (T_c), are more depleted than *volatile* elements, the elements with a lower T_c (e.g. Savage & Sembach 1996); (2) the depletions increase with the mean density of the medium (e.g. Savage & Bohlin 1979; Crinklaw, Federman & Joseph 1994). The depletion of an element X, is defined as:

$$\underbrace{\left[\frac{X_{\text{gas}}}{H} \right]}_{\text{depletion of X}} \equiv \underbrace{\log \left(\frac{X}{H} \right)_{\text{gas}}}_{\text{abundance of X}} - \underbrace{\log \left(\frac{X}{H} \right)_{\text{ref}}}_{\text{reference value}} \simeq \underbrace{\left[\frac{X_{\text{gas}}}{H} \right]_0}_{\text{minimum depletion}} + \underbrace{A_X \times F_\star}_{\text{local variation}}. \quad (4)$$

The second part of Equation (4) is a universal parameterization as a function of the depletion strength, F_\star (Jenkins 2009). The minimum depletion term is thought to correspond to the core of the grain, while the varying environmental factor, $A_X F_\star$, is attributed to accretion of mantles in denser environments.

Depletion measurements provide a direct estimate of the dust content, independent of model assumptions. In addition, they provide constraints on the stoichiometry through the number ratio of available elements. These measurements are however challenging. In the

Diffuse Neutral Medium (DNM), they are performed in absorption. Most of the transitions are in the UV, thus inaccessible from the ground. Apart from possible line saturation and ionization corrections, the most challenging aspect is the adoption of *reference abundances* (Equation 4), representing the total ISM (gas and dust) abundances. Indeed, the different standards (solar, meteoritic, F & G stars, *etc.*) exhibit some inconsistencies. Alternatively, H II region abundances can be estimated from nebular lines. These estimates rely on photoionization modelling, which add up another layer of uncertainties.

3.3.2. Extragalactic Depletions. In extragalactic systems, there are numerous studies of DNM depletions in damped Ly- α systems (DLA; *e.g.* De Cia et al. 2016) or in γ -ray bursts (*e.g.* Friis et al. 2015), facilitated by the redshifting of the transitions in the visible range. Although such studies are usually compelled to make corrections based on the MW, De Cia et al. (2016) adopted a holistic approach and derived self-consistent depletion sequences.

The depletions of several nearby galaxies have been studied. The most complete studies concern the Magellanic clouds, with several elements, along several individual sightlines (*e.g.* Roth & Blades 1997; Welty et al. 1997; Sembach et al. 2001; Sofia et al. 2006; Tchernyshyov et al. 2015; Jenkins & Wallerstein 2017). Reference abundances can be estimated *in situ*, directly from individual stars (*e.g.* Welty et al. 1997; Tchernyshyov et al. 2015). The main results are the following. (1) The LMC depletion pattern of most elements appears Galactic, the abundances being simply scaled down by the metallicity (Tchernyshyov et al. 2015). (2) In the SMC, there is a larger dynamics, likely resulting from more important processing (removal by shock waves). In addition, Si, Cr and Fe are systematically less depleted, with $[\text{Si}/\text{H}]_0$ consistent with 0 (Tchernyshyov et al. 2015). However, Jenkins & Wallerstein (2017)'s $[\text{Si}/\text{H}]_0$ is significantly larger than 0. Si depletion varies by a factor of $\simeq 2$ at nearly constant Fe depletions, suggesting a different condensation process (Tchernyshyov et al. 2015). (3) The C/O ratio is a factor of $\simeq 2$ below solar, in the Magellanic clouds, suggesting that the carbon-to-silicate grain mass fraction is lower (Table 2). (4) The Magellanic stream has a similar depletion pattern to the SMC (Sembach et al. 2001).

Other more extreme objects, like the lowest metallicity nearby galaxy IZw 18 (Aloisi et al. 2003; Lebouteiller et al. 2013), or several star forming galaxies (James et al. 2014) have been studied in absorption, with some uncertainties due to multiple sightlines with different physical conditions. Several studies based on H II emission lines focused on low- Z galaxies. It appears that $[\text{Mg}/\text{O}]$ and $[\text{Mg}/\text{S}]$ correlate with Z (Guseva et al. 2013), implying a higher Mg depletion at high Z . Similarly, $[\text{Fe}/\text{O}]$ correlates with Z (*e.g.* Rodríguez-Ardila, Contini & Viegas 2005; Izotov et al. 2006). These results are qualitatively consistent with the Magellanic cloud trends (Table 2).

3.4. Polarization Studies

Grains are one of the main agents polarizing light in galaxies. Historically, Hall (1949) and Hiltner (1949) first noted that starlight was sometimes polarized to a few percents, and that the degree of polarization was correlated with the reddening. Davis & Greenstein (1951) proposed that this polarization was caused by non-spherical grains. Stein (1966) predicted that the emission by such elongated grains should also produce polarized IR emission. Dolginov & Mitrofanov (1976) proposed radiative torques as the main mechanism of grain alignment. Recently, the whole sky polarization map of the Galaxy, at 353 GHz (1° resolution), has been observed by *Planck*. The submm polarization fraction can be as high

Table 2 Abundances and depletions in the Milky Way and the Magellanic clouds.

X	C	O	Mg	Si	Fe	Mass ratio
Milky Way						
$10^6 (X/H)_{\text{ref}}$	290^{+30}_{-20}	580^{+70}_{-60}	42^{+2}_{-2}	41^{+2}_{-2}	35^{+2}_{-2}	$Z_{\odot} = 1/75$
$[X_{\text{gas}}/H]_0$ (%)	23^{+27}_{-23}	$2.3^{+12.3}_{-2.3}$	46^{+3}_{-4}	40^{+5}_{-5}	89^{+1}_{-1}	$Z_{\text{dust}}^{(F_{\star}=0)} = 1/330$
$[X_{\text{gas}}/H]_0 + A_X$ (%)	39^{+9}_{-11}	42^{+7}_{-8}	95^{+1}_{-1}	96^{+1}_{-1}	99^{+1}_{-1}	$Z_{\text{dust}}^{(F_{\star}=1)} = 1/140$
LMC						
$10^6 (X/H)_{\text{ref}}$	87^{+25}_{-19}	320^{+90}_{-70}	18^{+4}_{-3}	22^{+6}_{-5}	21^{+4}_{-4}	$Z = 1/2 Z_{\odot}$
$[X_{\text{gas}}/H]_0$ (%)	$\simeq 31$	$\lesssim 20$...	52^{+3}_{-3}	89^{+1}_{-1}	$Z_{\text{dust}}^{(F_{\star}=0)} = 1/750$
$[X_{\text{gas}}/H]_0 + A_X$ (%)	94^{+1}_{-1}	99^{+1}_{-1}	$Z_{\text{dust}}^{(F_{\star}=1)} = 1/250$
SMC						
$10^6 (X/H)_{\text{ref}}$	33^{+9}_{-7}	140^{+30}_{-20}	$7.6^{+1.2}_{-1.1}$	$9.1^{+2.7}_{-2.0}$	$7.8^{+1.6}_{-1.4}$	$Z = 1/5 Z_{\odot}$
$[X_{\text{gas}}/H]_0$ (%)	$\simeq 28$	$\simeq 32$	49^{+6}_{-6}	40^{+3}_{-3}	89^{+1}_{-1}	$Z_{\text{dust}}^{(F_{\star}=0)} = 1/2760$
$[X_{\text{gas}}/H]_0 + A_X$ (%)	71^{+11}_{-18}	95^{+1}_{-1}	99^{+1}_{-1}	$Z_{\text{dust}}^{(F_{\star}=1)} = 1/630$

(MW) solar abundance compilation and depletions from [Jenkins \(2009\)](#). (LMC) stellar abundance compilation and depletions from [Tchernyshyov et al. \(2015\)](#); [C/H] and [O/H] from [Korn et al. \(2002\)](#). (SMC) stellar abundance compilation from [Tchernyshyov et al. \(2015\)](#); depletions from [Jenkins & Wallerstein \(2017\)](#); [C/H] from [Peña-Guerrero et al. \(2012\)](#)'s H II modelling of NGC 456; [O/H] derived from [Mallouris \(2003\)](#)'s [O/Zn] (Sk 108, $\log N(\text{H I}) = 20.5 \Rightarrow F_{\star} \simeq 0$) and [Jenkins & Wallerstein \(2017\)](#)'s [Zn/H]. Values in grey indicate an estimate from nebular emission lines.

as 20% in the most diffuse regions ($N(\text{H}) \simeq 10^{20} \text{ H cm}^{-2}$) and decreases along the densest sightlines ($N(\text{H}) \simeq 10^{22} \text{ H cm}^{-2}$; [Planck Collaboration et al. 2015a](#)). In the low density regime, this behaviour is consistent with turbulently disordered magnetic field orientations. In regions of higher densities, more opaque, the trend can be explained by the decrease of the efficiency of radiative torque alignment.

In nearby galaxies, polarization studies have been conducted at all wavelengths from the FUV to the radio. Dust-induced polarization is usually used to trace one of the three following phenomena.

3.4.1. The Geometry of Complex Regions. Polarization can provide information on the geometry of unresolved or poorly constrained sources. Most noticeably, the polarimetric observations of the central region of the archetypal Seyfert 2 galaxy, NGC 1068, were interpreted as the scattering of light from the central accretion disk, obscured by a dusty torus ([Antonucci & Miller 1985](#)). These results were a major step towards the unified AGN model, attributing the differences in observed properties of Seyfert galaxies to the difference in orientation of the central source ([Antonucci 1993](#)). Apart from AGN, the NIR polarimetry of M 82 has contributed revealing a central nuclear star forming ring ([Dietz et al. 1989](#)).

Polarization studies have also shed light on the nature of diffuse UV halos of star forming galaxies: are those made of purely scattered light, or is there a faint stellar population? The observations of edge-on galaxies, like NGC 3125 ([Alton et al. 1994](#)) or M 82 ([Yoshida, Kawabata & Ohyama 2011](#)) have revealed that their dusty outflows were scattering light from the central starburst. [Cole et al. \(1999\)](#) also studied the polarization of star forming regions in the LMC to constrain the extent of their UV halos.

3.4.2. The Structure of the Magnetic Field. In case of dichroic extinction or emission, the polarization angle provides a map of the projected magnetic field. Such studies were

DUST-INDUCED POLARIZATION PROCESSES

Scattering. The light from a bright source (star or AGN) scattered onto grains is partially polarized. The resulting fraction of linear polarization is a complex function of the dust composition, size and spatial distribution. This process is usually efficient in the UV (*e.g.* Zubko & Laor 2000). It applies to spherical and elongated grains, indifferently. Most radiative transfer models include this polarization mechanism.

Dichroic extinction. The light from a background source seen through a cloud of magnetically-aligned elongated grains is partially polarized, parallel to the magnetic field. In the MW, the wavelength-dependent linear polarization fraction, caused by this process, follows the Serkowski, Mathewson & Ford (1975) law. It is efficient from the Near-UV (NUV) to the NIR, peaking around $\lambda \simeq 0.55 \mu\text{m}$.

Dichroic emission. The thermal emission from magnetically-aligned elongated grains is polarized, perpendicular to the magnetic field. The wavelength-dependent fraction of linear polarization is rather flat over the whole FIR-to-submm regime (*e.g.* Guillet et al. 2017).

performed in the NIR/visible, among others, in NGC 891 (Montgomery & Clemens 2014), M82 (Greaves et al. 2000; Jones 2000), the SMC (Lobo Gomes et al. 2015), NGC 6946 (Fendt, Beck & Neininger 1998) and the dust lane of Cen A (Scarrott et al. 1996).

3.4.3. The Dust Composition. The wavelength-dependent shape of the polarization fraction provides valuable information on the dust constitution. In particular, studies of M31 (Clayton et al. 2004), M82 (Kawabata et al. 2014), the LMC (Clayton et al. 1996) and the SMC (Rodrigues et al. 1997) all concluded that the polarizing grains were smaller in these objects than in the MW. Polarimetry can also be used to discriminate models. For instance, Mason et al. (2007) studied the polarization of the 3.4 μm aliphatic band in order to test the silicate core/organic mantle model (Li & Greenberg 2002). They observed the interstellar medium of NGC 1068 in absorption towards its central engine. If the carriers of the 3.4 μm band were onto large grains, the feature would be significantly polarized, which is not the case.

3.5. Dust-Related Epiphenomena

3.5.1. Dust Observables in the X-Rays. Dust absorbs and scatters X-rays. First, the photoelectric absorption edges of elements locked-up in grains contain potential information on their chemical structure (*e.g.* Lee et al. 2009). For instance, Zeegers et al. (2017) studied the Si K-edge along the line of sight of a Galactic X-ray binary. They were able to constrain the column density and the chemical composition of the silicate grains. Second, X-ray scattering halos can be used to constrain dust models (*e.g.* Smith, Valencic & Corrales 2016). As an illustration, Corrales & Paerels (2015) modelled the X-ray halo around Cygnus X-3. They were able to put constraints on the size distribution, especially on the large grain cut-off. Lastly, Draine & Bond (2004) made a case that time-varying X-ray halo could be used to estimate distances of nearby galaxies, down to 1% accuracy for M31.

Among external galaxies, the dust-scattering X-ray halos of several γ -ray bursts have

been observed (*e.g.* Evans et al. 2014). However, to our knowledge, no such study has been conducted in nearby galaxies.

3.5.2. The Diffuse Interstellar Bands. DIBs are ubiquitous absorption features in the $\simeq 0.4 - 2 \mu\text{m}$ range. Over 400 of them have been detected in the ISM (Hobbs et al. 2009), since their discovery, a century ago (Heger 1922). They remain largely unidentified, although four of them have been attributed to C_{60}^+ (Campbell et al. 2015). They are associated to dust, as their strength correlates with $E(B - V)$ at low values, but they disappear in denser sightlines (*e.g.* Lan, Ménard & Zhu 2015). To first order, DIBs correlate with each other, but there are some notable differences, suggesting that they have different carriers (Herbig 1995). For instance, the so-called C_2 DIBs (Thorburn et al. 2003) appear to be found preferentially in diffuse molecular clouds.

DIBs are abundantly observed in external galaxies, including distant objects, like DLAs (*e.g.* Lawton et al. 2008). As a narrow spectral feature, they can easily be separated in velocity from the foreground Galactic features. They are observed in the ISM of nearby galaxies along the lines of sight of: **(1)** stars, in M33 (Cordiner et al. 2008), M31 (Cordiner et al. 2011) and the Magellanic clouds (*e.g.* Welty et al. 2006; van Loon et al. 2013; Bailey et al. 2015), among others; **(2)** SN II, in Cen A (Phillips et al. 1987; D’Odorico et al. 1989), M66 (Bolte et al. 1989), the LMC (Vidal-Madjar et al. 1987), M100 (Cox & Patat 2008), M82 (*e.g.* Welty et al. 2014), among others; **(3)** SN Ia (*e.g.* Sollerman et al. 2005; Huang et al. 2017); and **(4)** lenticular galaxies (Ritchey & Wallerstein 2015).

In solar metallicity, normal galaxies, the strengths of the DIBs and their relation to A_V seem to be similar to those of the MW (Heckman & Lehnert 2000; Sollerman et al. 2005; Cordiner et al. 2011; Huang et al. 2017), although some differences can be found (*e.g.* in M100, M33 and M82; Cox & Patat 2008; Cordiner et al. 2008; Welty et al. 2014). In contrast, the largest deviations are found in the Magellanic clouds. Welty et al. (2006) reported that the DIBs are weaker in the LMC and SMC, compared to the MW, by factors of $\simeq 7 - 9$ and $\simeq 20$, respectively. However, they found that the C_2 DIBs have the same strength per H atom as in the Galaxy. DIB spectra appear to be controlled by the UV field intensity (Cox et al. 2006), with disappearance of the features in the ionized gas or in high UV field (van Loon et al. 2013; Bailey et al. 2015). DIB strength also scales with metallicity, due to both lower shielding and lower elemental abundances (Cox et al. 2007; Bailey et al. 2015). Finally, DIBs appear to be linked with the shape of the extinction curve. Cox et al. (2007) demonstrated that the sightlines with weak or non-existent 2175 Å bump are those with weak or non-existent DIBs, in the SMC.

3.5.3. Grain Photoluminescence. Photoluminescence is a non-thermal emission process in which, subsequently to the absorption of a UV photon, a grain is brought to an excited electronic state. After partial internal relaxation, a redder photon is emitted, bringing the electron back to its fundamental state. The ERE, which is a broad emission band, found in the $\simeq 0.6 - 0.9 \mu\text{m}$ range of a diversity of Galactic environments, is attributed to dust photoluminescence (*e.g.* Witt & Vijh 2004). The nature of its carriers is still debated.

In nearby galaxies, ERE has been spectroscopically detected in the star forming region 30 Dor (LMC; Darbon, Perrin & Sivan 1998), in M82 (Perrin, Darbon & Sivan 1995) and NGC 4826 (Pierini et al. 2002). In the dwarf galaxies SBS 0335-052 and NGC 4449, Reines, Johnson & Hunt (2008) and Reines, Johnson & Goss (2008) modelled the photometric observations of several Super Star Clusters (SSC). Their result exhibit a significant *I-band*

excess that they attributed to ERE. However, Reines et al. (2010) admitted that this excess could be accounted for by continuum and line emission of the ionized gas, in NGC 4449.

3.5.4. The NIR Excess. An excess emission above the extrapolated stellar continuum is often detected in the NIR range (Joseph et al. 1984; Hunt & Giovanardi 1992). It is seen in disk galaxies (e.g. Lu et al. 2003; Boquien et al. 2011) and dwarf galaxies (e.g. Vanzi et al. 2000; Smith & Hancock 2009). It potentially hampers our ability to accurately estimate the stellar mass from NIR photometry. This excess could be due to: (1) nebular emission: Br α line and free-free continuum (e.g. Smith & Hancock 2009); (2) hot equilibrium dust (e.g. Vanzi et al. 2000), probably in circumstellar disks (Wood et al. 2008); (3) out-of-equilibrium small grains (e.g. Boquien et al. 2010).

Studying disk galaxies, Lu et al. (2003) describe this excess, having a color temperature of $\simeq 10^3$ K and an intensity of a few percent of the total FIR. They found this excess to correlate with the UIB intensity. In general, this excess correlates with SFR indicators (Boquien et al. 2010; Mentuch, Abraham & Zibetti 2010). The emissivity of the three proposed phenomena listed above correlates with star formation activity. In a filament of the BCD, NGC 1569, Onaka et al. (2010) showed spectroscopically that the nebular emission can not account for the excess, thus favoring hot dust.

3.5.5. The Submm Excess. An excess emission above the modelled dust continuum is often detected, longward $\simeq 500 \mu\text{m}$. The most significant reports of this *submm excess* can not be accounted for by (cf. Figure 1): free-free, synchrotron and molecular line emission (e.g. Galliano et al. 2003). The first occurrence of such an excess was unveiled by Reach et al. (1995), studying the COBE observations of the MW. Their IR-submm SED could be fitted with a MBB ($\beta = 2$; cf. Section 2.3.1.1), and an additional 4–7 K component. A few years later, Lisenfeld et al. (2002) and Galliano et al. (2003) found a statistically significant excess in the dwarf galaxy NGC 1569, at 850 μm and 1.3 mm. Several subsequent studies confirmed the presence of an excess in other late-type galaxies (e.g. Dumke, Krause & Wielebinski 2004; Bendo et al. 2006; Galametz et al. 2009), including the global SEDs of the Magellanic clouds (Israel et al. 2010; Bot et al. 2010). *Herschel* and *Planck* opened the way to more detailed tests. In particular, Paradis et al. (2012) showed that the 500 μm excess becomes significant in the peripheral regions of the MW ($> 35^\circ$), as well as towards some H II regions. Its relative amplitude can be up to $\simeq 20\%$. Spatially resolved observations of the LMC have shown that the 500 μm excess varies up to $\simeq 40\%$ in certain regions and is anticorrelated with the dust surface density (Galliano et al. 2011). When resolved in non-barred spirals, the *submm* excess is primarily detected in the disk outskirts, thus at low-surface density (e.g. Hunt et al. 2015).

COBE: COsmic
Background
Explorer
($\lambda = 12 - 5000 \mu\text{m}$;
1989 – 1993).

3.5.5.1. Reality of the phenomenon. First, we emphasize that, by definition, this excess is model-dependent. Different dust opacities lead to different amplitudes of the excess. For that reason, probing this excess with models which are not based on realistic optical properties is a non-sense. Second, the shape of the SED is well characterized in this regime. It has been observed at different wavelengths, with different instruments. It is still present with the latest *Herschel* calibration (Dale et al. 2017). In addition, reports of a deficit are very rare. Finally, Planck Collaboration et al. (2011a) showed that, while the *submm* excess in the integrated SED of the LMC was consistent with Cosmic Microwave Background (CMB) fluctuations, the SMC excess was significantly above this level.

3.5.5.2. Possible explanations. The origin of the excess is currently debated. The following explanations have been proposed.

Very cold dust (VCD) can be used to fit the excess. However, it leads to massive amounts of grains. Galliano et al. (2003) showed that VCD would be realistic only if this component was distributed in a few number of dense, parsec-size clumps. Using the spatially resolved observations of the 500 μm excess in the LMC, Galliano et al. (2011) concluded that this explanation is unrealistic.

Temperature dependent emissivity. The Meny et al. (2007) model predicts an increase of $\kappa(\lambda_0)$ and a decrease of β with the temperature of amorphous grains. It reproduces the MW excess (Paradis et al. 2012) and the LMC (Bot et al. 2010, coupled with spinning grains; cf. Section 3.5.6). However, it can not account for the excess in the SMC (Bot et al. 2010).

Magnetic grains. Draine & Hensley (2012) showed that the SMC excess could be attributed to magnetic nanoparticles (Fe, Fe_3O_4 , $\gamma\text{-Fe}_2\text{O}_3$). Thermal fluctuations in the magnetization of these grains can produce strong magnetic dipole emission, since ferromagnetic materials are known to have large opacities at microwave frequencies. This hypothesis seems to be consistent with the observed elemental abundances of the SMC and could also be responsible for the excess detected in other environments.

3.5.6. Spinning Grains. The AME is a cm continuum excess that can not be accounted for by the extrapolation of dust models, free-free, synchrotron and molecular line emission (Figure 1). It was first detected in the MW (Kogut et al. 1996). Draine & Lazarian (1998) promptly proposed that it was arising from the dipole emission of fastly rotating ultrasmall grains. The candidate carriers were thought to be PAHs. The WMAP and Planck data of the Galaxy were successfully fit with spinning dust models, including PAHs (e.g. Planck Collaboration et al. 2011b). In the MW, the AME correlates with all tracers of dust emission (Hensley, Draine & Meisner 2016). However, Hensley, Draine & Meisner (2016) showed that AME/TIR ratio does not correlate with the PAH abundance. These authors thus proposed that the carriers of the AME could be nano-silicates, rather than PAHs.

In nearby galaxies, the first unambiguous detection of an AME has been obtained in an outer region of NGC 6946 (Murphy et al. 2010; Scaife et al. 2010). Follow up observations showed evidence for AME in 8 regions of this galaxy (Hensley, Murphy & Staguhn 2015). This study showed that the spectral shape of this AME is consistent with spinning dust, but with a stronger AME-to-PAH-surface-density ratio, hinting that other grains could be the carriers. Overall, the AME fraction is highly variable, in nearby galaxies. Peel et al. (2011) put upper limits on the AME in M 82, NGC 253 and NGC 4945. These upper limits suggest that AME/100 μm is lower than in the MW, in these objects. In M 31, Planck Collaboration et al. (2015b) report a 2.3σ measurement of the AME, consistent with the Galactic properties. Finally, Bot et al. (2010), fitting the NIR-to-radio SED of the LMC and SMC, tentatively explained the submm/mm excess with the help of spinning dust, in combination with a modified submm dust emissivity (cf. Section 3.5.5). They conclude that if spinning grains are responsible for this excess, their emission must peak at 139 GHz (LMC) and 160 GHz (SMC), implying large ISRF intensities and densities. Draine & Hensley (2012) argued that such fastly rotating grains would need a PDR phase with a total luminosity more than two orders of magnitude brighter than the SMC.

WMAP: Wilkinson Microwave Anisotropy Probe ($\lambda \simeq 3.2 - 13$ mm; 2001 – 2010).

4. EVIDENCE OF DUST EVOLUTION

DUST EVOLUTION PROCESSES

Grain Formation. The dust mass is built up by: (1) grain condensation in the ejecta of core-collapse SNe and AGB stars. (2) grain (re-)formation in the ISM, by accretion of atoms and molecules (grain growth, and mantle and ice formation).

Grain Processing. The grain constitution is altered in the ISM by: (1) shattering and fragmentation by grain-grain collisions in low-velocity shocks (modification of the size distribution); (2) structural modifications by high energy photons or cosmic ray impacts; (3) coagulation.

Grain Destruction. The elements constituting the grains are partially or fully removed by: (1) erosion and evaporation by thermal or kinetic sputtering (gas-grain collision in a hot gas or a shock); (2) photodesorption of atoms and molecules; (3) thermal evaporation; (4) astration (incorporation into stars).

4.1. The Empirical Effects of Star Formation Activity & Metallicity

Dust evolution is the modification of the constitution of a grain mixture under the effect of environmental processing. Most dust evolution processes can be linked to star formation: (1) formation of molecular clouds and their subsequent evaporation; (2) stellar ejecta; (3) SN shock waves; (4) UV and high-energy radiation. The characteristic timescale of these processes is relatively short (of the order of the lifetime of massive stars; $\tau \lesssim 10$ Myr) and their effect is usually localized around the star forming region. For these reasons, the sSFR is an indicator of sustained dust processing. However, the dust lifecycle is a hysteresis. There is a longer term evolution, resulting from the progressive elemental enrichment of the ISM, which becomes evident on timescales of $\simeq 1$ Gyr. This evolutionary process can be traced by the metallicity.

These two evolutionary timescales have an impact on the integrated SEDs of nearby galaxies. Figure 7 illustrates that the effects of star formation activity and metallicity are not always easy to disentangle. Indeed, low- Z systems are often dominated by young stellar populations. In addition, their lower dust-to-gas mass ratio renders their ISM more transparent, and thus allows massive star formation to impact the ISM in a larger volume (cf. Section 2.1.3). In other words, some properties of dwarf galaxies may be the result of their hard and intense radiation field, rather than their low metallicity. In practice, dust evolution processes can be probed by comparing regions in a galaxy or by comparing integrated galaxies. Our ability to observe ISM dust evolution in real time is limited to SN remnants (*e.g.* SN 1987A; Dwek et al. 2010).

4.2. Localized Dust Processing

4.2.1. Grain Growth. There is clear evidence of FIR opacity variation in the MW. The main factor seems to be the density of the medium. For instance, Stepnik et al. (2003) found that the FIR dust cross-section per H atom increases by a factor of $\simeq 3$ from the diffuse ISM to

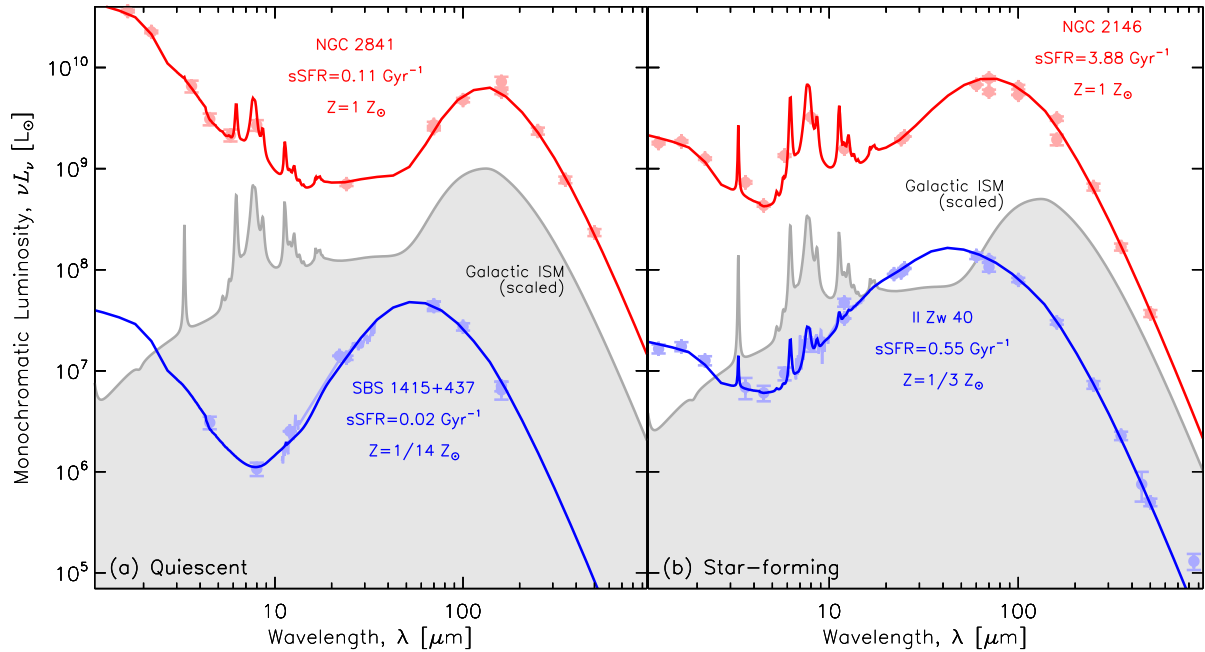


Figure 7

Effects of dust evolution on the SEDs of galaxies. Each panel displays the observations and the SED model of two nearby galaxies (Rémy-Ruyer et al. 2015), on top of the SED of the diffuse Galactic ISM (in grey). The red curve in panel (a) shows a quiescent solar metallicity galaxy. Apart from the stellar continuum, it is identical to the diffuse ISM. In contrast, the blue curve represents a low-metallicity quiescent system. Its dust properties are notably different: (1) weak or absent UIBs; (2) overall hotter dust (FIR peaks at shorter wavelengths); (3) a somehow broader FIR spectrum, resulting from a distribution of starlight intensities and/or an overabundance of small grains (cf. Section 2.3.1.2). This SED is qualitatively similar to the SED of a compact H II region (e.g. Peeters et al. 2002). The red curve in panel (b) shows a solar metallicity galaxy with a sustained star formation activity. Compared to its quiescent counterpart, it has a much hotter and broader FIR emission, originating at least partly in bright PDRs. The starbursting low- Z galaxy (blue curve in Figure 7-b) has the same features as its quiescent counterpart, with a broader FIR emission.

the molecular cloud they targeted. They noticed that this opacity variation is accompanied by the disappearance of the small grain emission. They concluded that grain coagulation could explain these variations (see also Köhler, Ysard & Jones 2015, hereafter K15). In the diffuse ISM, Ysard et al. (2015) showed that the variation of emissivity, including the $\beta - T$ relation (cf. Section 2.3.1.1), could be explained by slight variations of the mantle thickness of the J17 model. This observed behaviour is also consistent with the progressive de-mantling and disaggregation of molecular cloud-formed, mantled and coagulated grains injected into the low density ISM, following cloud disruption. It is perhaps not unreasonable to hypothesise that dust growth in the ISM occurs on short timescales during cloud collapse rather than by dust growth in the quiescent diffuse ISM. In this alternative interpretation, the arrow of time is in the opposite sense and requires rapid dust growth, through accretion and coagulation, in dense molecular regions and slow de-mantling and disaggregation in the diffuse ISM.

In nearby galaxies, such studies are difficult to conduct, as the emissivity variations are smoothed out by the mixing of dense and diffuse regions. Even, when potential evolutionary

trends are observed, their interpretation is often degenerate with other factors. The Magellanic clouds are the most obvious systems where this type of study can be attempted. The insights provided by depletion studies (cf. [Section 3.3](#)) show that there are clear variations of the fraction of heavy elements locked-up in dust, and these variations correlate with the density ([Tchernyshyov et al. 2015](#); [Jenkins & Wallerstein 2017](#)). Since the coagulation and the accretion of mantles lead to an increase of FIR emissivity (*e.g.* [K15](#)), we should expect emissivity variations in the Magellanic clouds. Indeed, [Roman-Duval et al. \(2017\)](#) studied the trends of gas surface density (derived from H I and CO) as a function of dust surface density (derived from the IR emission), in these galaxies. They found that the observed dust-to-gas mass ratio of the LMC increases smoothly by a factor of $\simeq 3$ from the diffuse to the dense regions. In the SMC, the same variation occurs, with a factor of $\simeq 7$. They argue that optically thick H I and CO-free H₂ gas (cf. [Section 2.4.2](#)) can not explain these trends, and that grain growth is thus the most likely explanation. However, we note that the possible increase of the dust opacity with density could explain part of this trend.

4.2.2. Size Distribution Variations. As we have seen in [Section 3.2](#), there is a great diversity of extinction curves in the MW and nearby galaxies. A large part of these variations is thought to be the result of variations in the size distribution, small R_V corresponding to an overabundance of small grains (*e.g.* [Cartledge et al. 2005](#)). Comparing the SMC bar to the SMC wing or the LMC2 supershell to the LMC average ([Figure 6](#)), it appears that there are more small grains in regions of massive star formation. In the same way, comparing the extinction curves in the MW, LMC and SMC, we also notice that there is a potential increase of the small grain fraction when the metallicity decreases. As pointed out in [Section 4.1](#), the two effects are degenerate.

Constraining the size distribution from the IR emission is more difficult due to the degeneracy between size and ISRF distributions (cf. [Section 2.3.1.2](#)). However, [Lisenfeld et al. \(2002\)](#) and [Galliano et al. \(2003\)](#) attempted the modelling of the IR SED of the dwarf galaxy NGC 1569, varying the size distribution. They both concluded that the dust in this object is dominated by nano-grains. Interestingly enough, the extinction curve corresponding to the grain properties of [Galliano et al. \(2003\)](#) was qualitatively similar to the SMC, with a steep FUV-rise and a weak bump. [Galliano et al. \(2005\)](#) found the same result for three other dwarf galaxies. In the LMC, [Paradis et al. \(2009\)](#) also concluded to a drastic increase of the fraction of very small grains, especially around 30 Dor. It is possible that, even if a fraction of hot equilibrium dust has been mistaken for small grains by these studies, these systems harbor, on average, smaller grains than normal galaxies. SN-triggered shock waves, which are abundant in star forming dwarf galaxies (cf. [Section 2.1.3](#)), by fragmenting large grains, could explain the peculiar SEDs and extinction curves of dwarf galaxies (*e.g.* [Fig. 17 of Bocchio, Jones & Slavin 2014](#), $V_{\text{shock}} = 100 \text{ km s}^{-1}$).

4.2.3. Grain Destruction. The dust destruction efficiency in SN-triggered shock waves was recently re-estimated using the J17 model to evaluate the role of dust mantles, and to calculate the emission and extinction from shocked dust ([Bocchio, Jones & Slavin 2014](#)). Further constraints were put on the silicate destruction time, using hydrodynamical simulations ([Slavin, Dwek & Jones 2015](#)). The main conclusions of these studies are the following. (1) a-C(:H) grains are quickly destroyed, even in a 50 km s^{-1} shock, which is counter to earlier work (*e.g.* [Jones, Tielens & Hollenbach 1996](#)) that used the properties of graphite and an amorphous carbon other than a-C(:H). It implies that the re-formation of carbonaceous

dust in the dense regions of the ISM is a strong requirement (cf. Section 4.2.1). (2) Silicate grains appear to be more resilient, with a mean lifetime of $\tau_{\text{sil}} \simeq 2 - 3$ Gyr (Slavin, Dwek & Jones 2015), one order of magnitude larger than the previous estimate of $\tau_{\text{sil}} \simeq 400$ Myr (Jones, Tielens & Hollenbach 1996).

4.2.3.1. Photodestruction of small grains. In Galactic PDRs, Boulanger et al. (1998, Fig. 3) showed that the UIB strength departs from a linear dependence on the ISRF intensity, U , for $U \gtrsim 1000$, indicating that band carrier destruction has occurred. It therefore implies that, in a galaxy with regions of intense stellar radiation, the observed UIBs are most likely not coming from high ISRF regions. More recently, work on radiative transfer modelling of the dust emission in Galactic PDRs has shown that the small grains are significantly under abundant, with respect to the diffuse ISM (Arab et al. 2012).

This phenomenon is widely observed in nearby galaxies. First, the UIB carriers appear cleared out of the hotter parts of extragalactic, star forming regions (e.g. Galametz et al. 2013; Wu et al. 2015). This destruction impacts a larger volume in blue compact galaxies. For example, in NGC 5253, the $11.3 \mu\text{m}$ equivalent width increases with the distance from the SSC region, over several hundreds of parsecs (Beirão et al. 2006). Second, the $L_{3.3}/L_{\text{IR}}$ ratio of LIRGs and ULIRGs decreases when L_{IR} increases (e.g. Imanishi et al. 2010). Since L_{IR} quantifies the SFR (cf. Section 2.4.1), this relation indicates that the UIB destruction can be seen at the scale of the whole galaxy. Finally, there are well-known correlations between the UIB equivalent width and various tracers of the intensity and hardness of the radiation field, such as the ionic line ratio $[\text{Ne III}]_{15.56\mu\text{m}}/[\text{Ne II}]_{12.81\mu\text{m}}$ (Madden et al. 2006; Gordon et al. 2008; Lebouteiller et al. 2011). These correlations are observed both within spatially resolved sources and among integrated galaxies. These results suggests that scaling a diffuse ISM-type dust emission to regions of enhanced radiation field, such as in Figure 3-c, is not appropriate.

4.2.3.2. Sputtering: grain evolution in hot plasmas. The superwind of M 82 exhibits filaments of dust and gas around the central outflows. PAHs or carbonaceous nano-particles embedded in such energetic regions would be exposed to soft X-rays ($0.5 - 2.0$ keV) and a hot gas ($T_{\text{gas}} \simeq 10^7$ K; Section 2.1.5). In such regions, their survival time is only $\simeq 20$ Myr, and that their destruction is principally due to collisions with the hot gas rather than by X-ray photo-destruction (Micelotta, Jones & Tielens 2010). Yet, UIBs are detected in these outflows (e.g. Yamagishi et al. 2012; Beirão et al. 2015). Thus, they are likely protected in the entrained cold gas that is being ablated into the hot outflowing gas, rather than present in the hot gas itself (Micelotta, Jones & Tielens 2010; Bocchio et al. 2012, 2013).

4.3. Cosmic Dust Evolution

4.3.1. Dust-Related Scaling Relations. The correlation between combinations of global parameters, such as M_{dust} , M_{gas} , M_{star} or SFR, across galaxy types, provides observational clues of cosmic evolution. Dust-related scaling relations have thrived on *Herschel* data, as this observatory has provided reliable dust mass estimates for statistical samples of galaxies, with various selection criteria (e.g. Cortese et al. 2012; Rémy-Ruyer et al. 2015; Clark et al. 2015; De Vis et al. 2017a). Figure 8-a displays the evolution of the dust-to-gas mass ratio, as a function of the specific gas mass. When a galaxy evolves, its gas content is converted into stars, reducing the $M_{\text{gas}}/M_{\text{star}}$ ratio. At the same time, the ISM is enriched

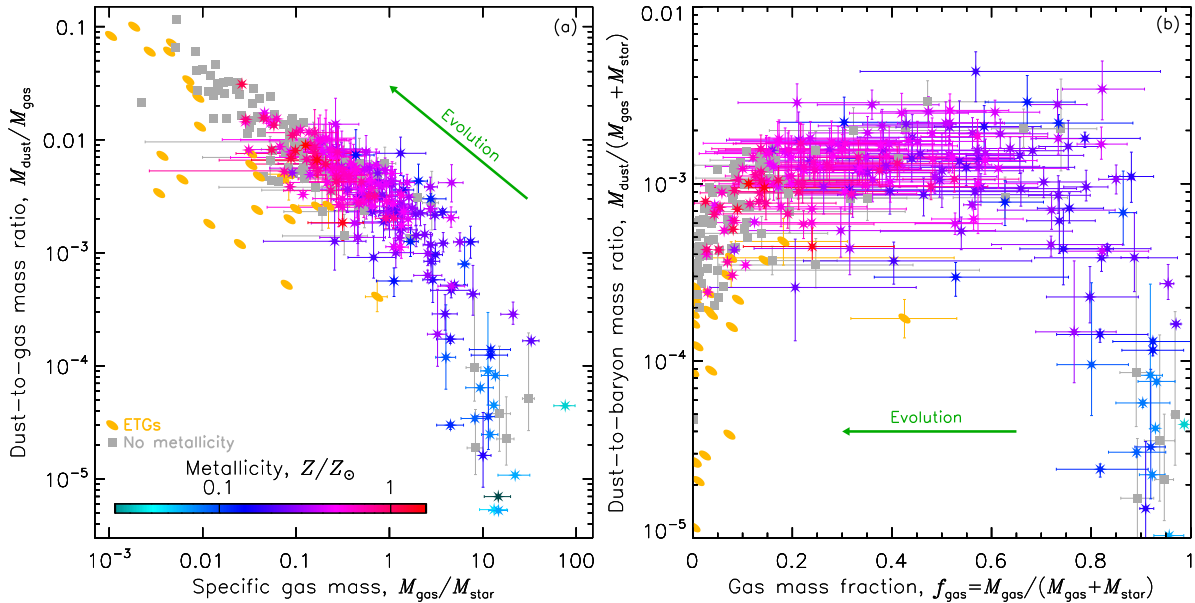


Figure 8

Main scaling relations. Each point represents a nearby galaxy from the volume-limited samples of De Vis et al. (2017a, H I-selected), Clark et al. (2015, 250 μm -selected), Cortese et al. (2012, K-band-selected) and Rémy-Ruyer et al. (2015, Z-selected), homogenized by De Vis et al. (2017b). In both panels, the galaxies are color coded with metallicity, when available. The gas mass is estimated with the sole neutral atomic tracer ($M_{\text{gas}} \simeq 1.32M_{\text{H I}}$, accounting for He).

in dust, increasing the $M_{\text{dust}}/M_{\text{gas}}$ ratio. We also see that Early-Type Galaxies (ETG), which are X-ray bright sources, lie notably below the correlation. This is possibly the result of thermal sputtering of the grains in a hot plasma ($T \gtrsim 10^6$ K; De Vis et al. 2017a). Figure 8-b demonstrates the effect of astration on the dust content. It shows the dust build-up, early-on ($f_{\text{gas}} \gtrsim 0.8$), then a plateau, and a net mass loss at ($f_{\text{gas}} \lesssim 0.2$).

4.3.2. Dust-to-Gas Mass Ratio Evolution with Metallicity. An important scaling relation, often used to constrain dust evolution models, is the trend of dust-to-gas mass ratio with metallicity (e.g. Lisensfeld & Ferrara 1998; Draine et al. 2007; Galliano, Dwek & Chaniai 2008; Rémy-Ruyer et al. 2014; De Vis et al. 2017b). Figure 9-a shows this relation for nearby galaxies (in blue). It is clearly non-linear, suggesting that dust production is less efficient at early stages. There are several sources of uncertainties that could bias this relation. (1) To derive the dust mass, the dust constitution has been assumed homogeneous throughout the whole sample. However, the expected variations of the grain mixture constitution (cf. Section 4.2.1) could alter the dust mass by a factor $\simeq 2 - 3$ (K15), which is only a minor effect on a trend spanning four orders of magnitude. (2) The estimate of the gas mass could be inaccurate. In particular, the absence of molecular gas mass constraints is problematic. However, we note that Rémy-Ruyer et al. (2014) using CO-derived H_2 masses and exploring the effects of different CO-to- H_2 conversion factors, found a similar trend. As noted by De Vis et al. (2017a), the displayed sample is not H_2 -dominated, and the uncertainty on the total gas mass is not expected to be larger than a factor of $\simeq 2$.

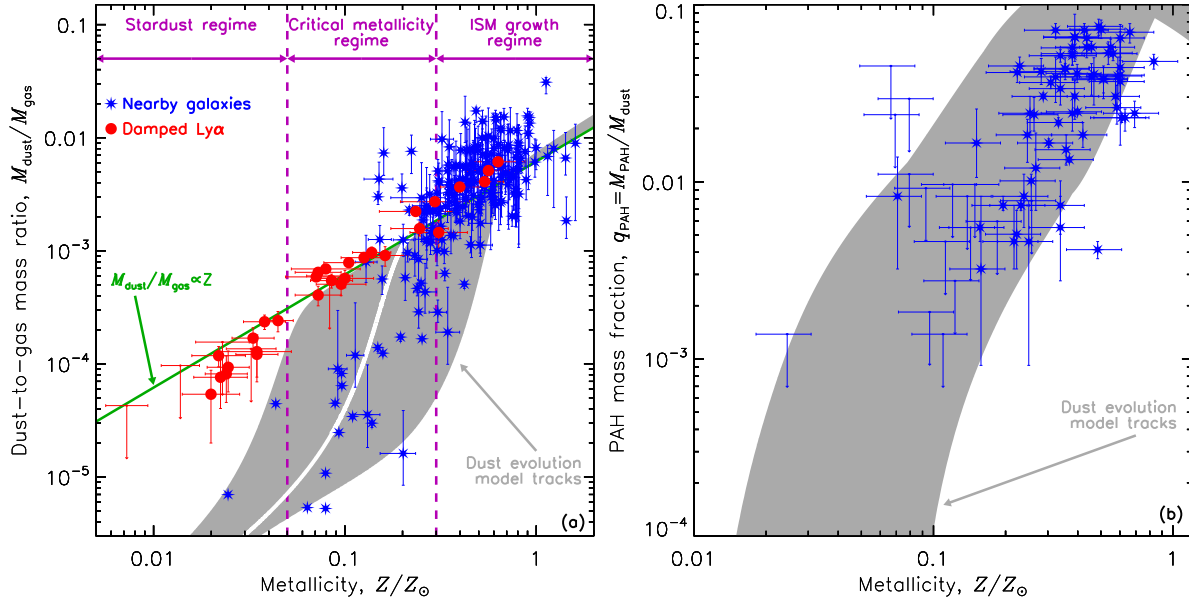


Figure 9

Dust evolution with metallicity. (a) Total dust-to-gas mass ratios of nearby galaxies (De Vis et al. 2017b) and DLAs (De Cia et al. 2016). The grey area represents the tracks of the model of Asano et al. (2013), varying the star formation timescale from $\tau_{\text{SF}} = 0.5$ to 50 Gyr ($\tau_{\text{SF}} = 5$ Gyr in white). The green line shows the locus of a constant, Galactic dust-to-metal mass ratio. (b) PAH-to-dust mass ratios for the nearby galaxy sample of Rémy-Ruyer et al. (2015). The grey area shows the tracks of the G08a dust evolution model. The metallicity, Z , has been derived from the O abundance.

(3) Low-metallicity galaxies usually have large HI halos surrounding their dust emitting region (cf. Section 2.1.3). A dust-to-gas mass ratio encompassing the whole halo would therefore be underestimated (see the discussion in Draine et al. 2007; Rémy-Ruyer et al. 2014). Although, this effect has been partially corrected for by Rémy-Ruyer et al. (2014), based on the available HI maps of their sample. In particular, the HI mass of the lowest metallicity source in Figure 9-a, IZw 18, has been corrected. It is therefore difficult to understand how the non-linearity of the trend would result from sole measurement biases.

We compare the nearby galaxy trend to the DLA sample of De Cia et al. (2016), in Figure 9-a. The dust-to-gas mass ratio and the metallicity of DLAs are all estimated from redshifted UV absorption lines (Section 3.3). These sources show an almost perfectly linear trend down to $\simeq 1/100 Z_{\odot}$. Their dust-to-metal mass ratio varies by only a factor of $\simeq 3$ over the whole metallicity range.

4.3.3. Models of Global Dust Evolution. It is possible to model the dust evolution of a galaxy, over cosmic time, by accounting for the balance between the production and destruction mechanisms. This approach was initiated by Dwek & Scalo (1980), who included grain processing in gas enrichment models. The main physical ingredients are the following. (1) The star formation history of the galaxy is the driving mechanism. It can be parameterized, with different time-scales, episodic bursts or can be regulated by the inflow and outflow rates. (2) At a given time, different stellar populations are born (IMF dependent), they destroy a fraction of the dust by astration. (3) At the end of their lifetime, stars inject

newly formed heavy elements and dust in the **ISM**. The stellar yields of core-collapse **SNe** and **AGB** stars are however quite uncertain (see the discussion in [Matsuura et al. 2015](#)). (4) Grains grow in the **ISM**, by accretion. However, the associated sticking coefficients are uncertain. (5) Finally, as massive stars die, dust is destroyed by their **SN**-triggered shock waves, whose efficiency is also uncertain (cf. [Section 4.2.3](#)). Most studies develop one-zone models. The evolution of the size distribution can be tracked (*e.g.* [Hirashita 2015](#)).

Despite the noted uncertainty in the efficiency of the individual processes, these models provide consistent trends of dust-to-gas ratio with metallicity, which enlighten the observations discussed in [Section 4.3.2](#). We display the area covered by different dust evolution tracks in [Figure 9-a](#). These tracks correspond to different star formation histories. We can see that they describe remarkably the nearby galaxy distribution. They can be characterized by the three following regimes. (1) At low- Z , the grains are mainly condensed in stellar ejecta, the dust-to-gas ratio is proportional to metallicity, but with a low dust-to-metal ratio. (2) At intermediate metallicities, grain growth in the **ISM** starts to become important, as there are more heavy elements to be accreted. The overall dust production efficiency increases. (3) At metallicity close to solar, we reach a linear regime, dominated by grain growth. The nearby galaxy trend in [Figure 9-a](#) therefore suggests that grain growth is a crucial process (see also [Section 4.2.3](#)). The scatter among the different objects can be explained by different star formation histories. On the contrary, the **DLA** trend does not seem to agree with the displayed dust evolution models. This disagreement is currently debated. It might be due to the particular history of these systems. For example, it is possible to have a quasi-linear trend, down to low- Z , with an episodic star formation history ([Zhukovska 2014](#)).

4.3.4. The Aromatic Feature Strength Evolution with Metallicity. The **UIB** equivalent width clearly rises with metallicity. It was first demonstrated by [Engelbracht et al. \(2005\)](#), using broadband photometry, and by [Madden et al. \(2006\)](#), with spectroscopic observations. [Engelbracht et al. \(2005\)](#) argued that there were two regimes: a high **UIB** fraction above $\simeq 1/5 - 1/3 Z_{\odot}$; and a low value, below. However, [Galliano, Dwek & Chantal \(2008, hereafter G08a\)](#) demonstrated that this was a bias, due to the fact that the continuum dominates the **MIR** broadbands when the **UIB** strength becomes weak. Trends constrained with spectroscopy appear rather smooth, although there is significant scatter ([Figure 9-b](#)). It was rapidly proposed that the origin of this phenomenon was the enhanced destruction of the **UIB** carriers in the **UV** permeated **ISM** of dwarf galaxies (cf. [Section 4.2.3.1](#)), illustrating again the degeneracy between star formation activity and metallicity (cf. [Section 4.1](#)). Indeed, the **UIB** strength appears slightly better correlated with tracers of the **ISRF** hardness than with metallicity (*e.g.* [Gordon et al. 2008](#); [Wu, Hogg & Moustakas 2011](#)).

UIB carrier destruction is indubitably an important process in low- Z systems, but it does not exclude the possible deficiency of their formation. [G08a](#) hypothesized that the **UIB** carriers could be mostly produced by the long-lived **AGB** stars. This delayed injection mechanism could explain the trend (tracks on [Figure 9-b](#)). However, as we have seen in [Section 4.2.3](#), the **UIB** carriers are very volatile and need to reform in the **ISM**. Alternatively, [Seok, Hirashita & Asano \(2014\)](#) showed that a dust evolution model in which **PAHs** are formed by fragmentation of large carbonaceous grains can explain the observed **PAH** trend. Observationally, [Sandstrom et al. \(2010\)](#), modelling the **MIR** spectra of several regions in the **SMC**, found that the **PAH** mass fraction correlates better with the molecular gas. They proposed that **PAHs** could form in molecular clouds. The trend with metallicity would then

result from the lower filling factor of the molecular gas at low- Z . This interesting scenario is probably not complete, as the PAH fractions they find in shielded regions are still a factor of $\simeq 2 - 4$ lower than in the MW. This is not surprising as the C/O ratio is about twice lower in the SMC (Table 2). There is no simple answer to this open question, but it appears that to explain the paucity of UIBs in low- Z environments, one needs to articulate their photodestruction with the deficiency of their formation process.

FUTURE CHALLENGES

1. Current dust models do not provide a parameterization of the grain mixture constitution as a function of the physical conditions. As we have discussed, local evolution processes, like the photodestruction of small grains or the mantle growth and evaporation, bias our interpretations, when using models with a fixed constitution. Working towards being able to predict, even in a simplified way, the grain properties for an arbitrary gas density and ISRF intensity, is necessary to interpret the already existing observations.
2. We are now at a time where nearby galaxies have been observed in detail, over the whole electromagnetic spectrum. We are thus compelled to think beyond integrated broadband fluxes to go on progressing.

Spatially resolved studies ($\lesssim 1''$) are possible in the MIR, with *JWST*, and in the submm, with *ALMA*. These could help resolve the dust heating in dense extragalactic PDRs (Equation 1) and thus provide constraints on the dust properties in high ISRF conditions.

FIR spectroscopy (*SPICA*) would be valuable for: (1) better constraining the shape of the SED; and (2) identifying new solid state features.

Multi-process studies are the key to solving the degeneracies inherent to dust models. *LUVVOIR* could provide valuable constraints on the extinction, depletion, DIBs and ERE of regions or galaxies which have been observed with the previous IR-submm telescopes.

3. The increase in sensitivity of the next generation of instruments will be a challenge for data analysis methods. More precise fluxes will require proper accounts of foreground and background emissions, especially if we are interested in the diffuse ISM of galaxies. More complex spatial and spectral decomposition methods, with rigorous treatment of the uncertainties, will be necessary.

JWST: NIR-MIR
space telescope
($\lambda \simeq 0.6 - 27 \mu\text{m}$;
launch in 2019),
with sub-arcsec
resolution.

SPICA: MIR-FIR
space telescope
($\lambda \simeq 12 - 210 \mu\text{m}$;
launch in $\simeq 2025$),
with unprecedented
sensitivity.

LUVVOIR: UV-NIR
space telescope (in
preparation).

DISCLOSURE STATEMENT

The authors are not aware of any affiliations, memberships, funding, or financial holdings that might be perceived as affecting the objectivity of this review.

ACKNOWLEDGMENTS

We thank Vincent Guillet for providing us with the polarization model of Figure 1, Ilse De Looze for Figure 2, Timoth e Roland and Ronin Wu for the data of Figure 5-a, and Pieter

De Vis for the data in [Figure 8](#). We thank Maarten Baes, Diane Cormier, Pieter De Vis, Vincent Guillet, Sacha Hony, Vianney Lebouteiller, Suzanne Madden, Takashi Onaka and Sébastien Viaene, for useful discussions and comments, as well as the scientific editor, Bruce Draine. We acknowledge support from the EU FP7 project DustPedia (Grant No. 606847). F.G. acknowledges support by the Agence Nationale pour la Recherche through the program SYMPATICO (Projet ANR-11-BS56-0023) and the PRC 1311 between CNRS and JSPS. M.G. acknowledges funding from the European Research Council (ERC) under the European Union Horizon 2020 programme (MagneticYSOs project, grant No 679937).

LITERATURE CITED

- Allamandola LJ, Tielens AGGM, Barker JR. 1985. *ApJ* 290:L25–L28
- Aloisi A, Savaglio S, Heckman TM, Hoopes CG, Leitherer C, Sembach KR. 2003. *ApJ* 595:760–778
- Alton PB, Draper PW, Gledhill TM, Stockdale DP, Scarrott SM, Wolstencroft RD. 1994. *MNRAS* 270:238
- Alton PB, Trehwella M, Davies JI, Evans R, Bianchi S, et al. 1998. *A&A* 335:807–822
- Alton PB, Xilouris EM, Bianchi S, Davies J, Kylafis N. 2000. *A&A* 356:795–807
- Alton PB, Xilouris EM, Misiriotis A, Dasyra KM, Dumke M. 2004. *A&A* 425:109–120
- Amanullah R, Goobar A, Johansson J, Banerjee DPK, Venkataraman V, et al. 2014. *ApJ* 788:L21
- Aniano G, Draine BT, Calzetti D, Dale DA, Engelbracht CW, et al. 2012. *ApJ* 756:138
- Antonucci R. 1993. *ARA&A* 31:473–521
- Antonucci RRJ, Miller JS. 1985. *ApJ* 297:621–632
- Arab H, Abergel A, Habart E, Bernard-Salas J, Ayasso H, et al. 2012. *A&A* 541:A19
- Asano RS, Takeuchi TT, Hirashita H, Inoue AK. 2013. *Earth, Planets, and Space* 65:213–222
- Baes M, Davies JI, Dejonghe H, Sabatini S, Roberts S, et al. 2003. *MNRAS* 343:1081–1094
- Baes M, Fritz J, Gadotti DA, Smith DJB, Dunne L, et al. 2010. *A&A* 518:L39
- Bailey M, van Loon JT, Sarre PJ, Beckman JE. 2015. *MNRAS* 454:4013–4026
- Battisti AJ, Calzetti D, Chary RR. 2016. *ApJ* 818:13
- Beirão P, Armus L, Lehnert MD, Guillard P, Heckman T, et al. 2015. *MNRAS* 451:2640–2655
- Beirão P, Brandl BR, Devost D, Smith JD, Hao L, Houck JR. 2006. *ApJ* 643:L1–L4
- Bendo GJ, Boselli A, Dariush A, Pohlen M, Roussel H, et al. 2012. *MNRAS* 419:1833–1859
- Bendo GJ, Dale DA, Draine BT, Engelbracht CW, Kennicutt Jr. RC, et al. 2006. *ApJ* 652:283–305
- Bendo GJ, Draine BT, Engelbracht CW, Helou G, Thornley MD, et al. 2008. *MNRAS* 389:629–650
- Bendo GJ, Joseph RD, Wells M, Gallais P, Haas M, et al. 2002. *AJ* 123:3067–3107
- Bendo GJ, Wilson CD, Pohlen M, Sauvage M, Auld R, et al. 2010. *A&A* 518:L65
- Berlind AA, Quillen AC, Pogge RW, Sellgren K. 1997. *AJ* 114:107–114
- Bianchi L, Clayton GC, Bohlin RC, Hutchings JB, Massey P. 1996. *ApJ* 471:203
- Bianchi S. 2007. *A&A* 471:765–773
- Bianchi S. 2008. *A&A* 490:461–475
- Block DL, Puerari I, Elmegreen BG, Bournaud F. 2010. *ApJ* 718:L1–L6
- Block DL, Witt AN, Grosbol P, Stockton A, Moneti A. 1994. *A&A* 288:383–395
- Bocchio M, Bianchi S, Hunt LK, Schneider R. 2016. *A&A* 586:A8
- Bocchio M, Jones AP, Slavin JD. 2014. *A&A* 570:A32
- Bocchio M, Jones AP, Verstraete L, Xilouris EM, Micelotta ER, Bianchi S. 2013. *A&A* 556:A6
- Bocchio M, Micelotta ER, Gautier AL, Jones AP. 2012. *A&A* 545:A124
- Bolte M, Saddlemeyer L, Mendes de Oliveira C, Hodder P. 1989. *PASP* 101:921–924
- Boquien M, Calzetti D, Combes F, Henkel C, Israel F, et al. 2011. *AJ* 142:111
- Boquien M, Duc PA, Galliano F, Braine J, Lisenfeld U, et al. 2010. *AJ* 140:2124–2144
- Boselli A, Ciesla L, Buat V, Cortese L, Auld R, et al. 2010. *A&A* 518:L61
- Boselli A, Ciesla L, Cortese L, Buat V, Boquien M, et al. 2012. *A&A* 540:A54

- Boselli A, Sauvage M, Lequeux J, Donati A, Gavazzi G. 2003. *A&A* 406:867–877
- Bot C, Ysard N, Paradis D, Bernard JP, Lagache G, et al. 2010. *A&A* 523:A20+
- Boudet N, Mutschke H, Nayral C, Jäger C, Bernard JP, et al. 2005. *ApJ* 633:272–281
- Boulanger F, Abergel A, Bernard JP, Cesarsky D, Puget JL, et al. 1998. *The Nature of Small Interstellar Dust Particles*. In *Star Formation with the Infrared Space Observatory*, eds. J Yun, L Liseau, vol. 132 of *Astronomical Society of the Pacific Conference Series*
- Boulanger F, Perault M. 1988. *ApJ* 330:964–985
- Bressan A, Panuzzo P, Buson L, Clemens M, Granato GL, et al. 2006. *ApJ* 639:L55–L58
- Calzetti D. 2001. *PASP* 113:1449–1485
- Calzetti D, Armus L, Bohlin RC, Kinney AL, Koornneef J, Storchi-Bergmann T. 2000. *ApJ* 533:682–695
- Calzetti D, Kennicutt RC, Engelbracht CW, Leitherer C, Draine BT, et al. 2007. *ApJ* 666:870–895
- Calzetti D, Kinney AL, Storchi-Bergmann T. 1994. *ApJ* 429:582–601 (C94)
- Campbell EK, Holz M, Gerlich D, Maier JP. 2015. *Nature* 523:322–323
- Cardelli JA, Clayton GC, Mathis JS. 1989. *ApJ* 345:245–256 (C89)
- Cartledge SIB, Clayton GC, Gordon KD, Rachford BL, Draine BT, et al. 2005. *ApJ* 630:355–367
- Chevance M, Madden SC, Lebouteiller V, Godard B, Cormier D, et al. 2016. *A&A* 590:A36
- Clark CJR, Dunne L, Gomez HL, Maddox S, De Vis P, et al. 2015. *MNRAS* 452:397–430
- Clayton GC, Gordon KD, Bianchi LC, Massa DL, Fitzpatrick EL, et al. 2015. *ApJ* 815:14
- Clayton GC, Gordon KD, Salama F, Allamandola LJ, Martin PG, et al. 2003. *ApJ* 592:947–952
- Clayton GC, Green J, Wolff MJ, Zellner NEB, Code AD, et al. 1996. *ApJ* 460:313
- Clayton GC, Wolff MJ, Gordon KD, Smith PS, Nordsieck KH, Babler BL. 2004. *AJ* 127:3382–3387
- Clements DL, Sutherland WJ, McMahon RG, Saunders W. 1996. *MNRAS* 279:477–497
- Cole AA, Nordsieck KH, Gibson SJ, Harris WM. 1999. *AJ* 118:2280–2291
- Combes F, Boquien M, Kramer C, Xilouris EM, Bertoldi F, et al. 2012. *A&A* 539:A67
- Conroy C, Schiminovich D, Blanton MR. 2010. *ApJ* 718:184–198 (C10)
- Contursi A, Poglitsch A, Grácia Carpio J, Veilleux S, Sturm E, et al. 2013. *A&A* 549:A118
- Cordiner MA, Cox NLJ, Evans CJ, Trundle C, Smith KT, et al. 2011. *ApJ* 726:39
- Cordiner MA, Smith KT, Cox NLJ, Evans CJ, Hunter I, et al. 2008. *A&A* 492:L5–L8
- Cormier D, Madden SC, Lebouteiller V, Abel N, Hony S, et al. 2015. *A&A* 578:A53
- Corrales LR, Paerels F. 2015. *MNRAS* 453:1121–1135
- Cortese L, Ciesla L, Boselli A, Bianchi S, Gomez H, et al. 2012. *A&A* 540:A52
- Cox NLJ, Cordiner MA, Cami J, Foing BH, Sarre PJ, et al. 2006. *A&A* 447:991–1009
- Cox NLJ, Cordiner MA, Ehrenfreund P, Kaper L, Sarre PJ, et al. 2007. *A&A* 470:941–955
- Cox NLJ, Patat F. 2008. *A&A* 485:L9–L12
- Crenshaw DM, Kraemer SB, Bruhweiler FC, Ruiz JR. 2001. *ApJ* 555:633–640
- Crinklaw G, Federman SR, Joseph CL. 1994. *ApJ* 424:748–753
- Crocker AF, Calzetti D, Thilker DA, Aniano G, Draine BT, et al. 2013. *ApJ* 762:79
- Croxall KV, Smith JD, Wolfire MG, Roussel H, Sandstrom KM, et al. 2012. *ApJ* 747:81
- da Cunha E, Charlot S, Elbaz D. 2008. *MNRAS* 388:1595–1617
- Dalcanton JJ, Fouesneau M, Hogg DW, Lang D, Leroy AK, et al. 2015. *ApJ* 814:3
- Dale DA, Cook DO, Roussel H, Turner JA, Armus L, et al. 2017. *ApJ* 837:90
- Dale DA, Helou G, Contursi A, Silbermann NA, Kolhatkar S. 2001. *ApJ* 549:215–227
- Darbon S, Perrin JM, Sivan JP. 1998. *A&A* 333:264–268
- Dasyra KM, Xilouris EM, Misiriotis A, Kylafis ND. 2005. *A&A* 437:447–456
- Davies JI, Alton P, Trewhella M, Evans R, Bianchi S. 1999. *MNRAS* 304:495–500
- Davies JI, Trewhella M, Jones H, Lisk C, Madden A, Moss J. 1997. *MNRAS* 288:679–690
- Davis Jr. L, Greenstein JL. 1951. *ApJ* 114:206
- De Cia A, Ledoux C, Mattsson L, Petitjean P, Srianand R, et al. 2016. *A&A* 596:A97
- De Geyter G, Baes M, De Looze I, Bendo GJ, Bourne N, et al. 2015. *MNRAS* 451:1728–1739
- De Looze I, Baes M, Bendo GJ, Ciesla L, Cortese L, et al. 2012a. *MNRAS* 427:2797–2811

- De Looze I, Baes M, Fritz J, Verstappen J. 2012b. *MNRAS* 419:895–903
- De Marchi G, Panagia N. 2014. *MNRAS* 445:93–106
- De Vis P, Dunne L, Maddox S, Gomez HL, Clark CJR, et al. 2017a. *MNRAS* 464:4680–4705
- De Vis P, Gomez HL, Schofield SP, Maddox S, Dunne L, et al. 2017b. *ArXiv e-prints*
- Deshmukh SP, Tate BT, Vagshette ND, Pandey SK, Patil MK. 2013. *Research in Astronomy and Astrophysics* 13:885–898
- Devereux NA, Young JS. 1990. *ApJ* 359:42–56
- Dewangan GC, Singh KP, Bhat PN. 1999. *AJ* 118:785–796
- Dietz RD, Gehrz RD, Jones TJ, Grasdalen GL, Smith J, et al. 1989. *AJ* 98:1260–1264
- Disney M, Davies J, Phillipps S. 1989. *MNRAS* 239:939–976
- Dobashi K, Bernard JP, Hughes A, Paradis D, Reach WT, Kawamura A. 2008. *A&A* 484:205–223
- D’Odorico S, di Serego Alighieri S, Pettini M, Magain P, Nissen PE, Panagia N. 1989. *A&A* 215:21–32
- Dolginov AZ, Mitrofanov IG. 1976. *Ap&SS* 43:291–317
- Dong H, Li Z, Wang QD, Lauer TR, Olsen K, et al. 2014. *ApJ* 785:136
- Draine BT. 1978. *ApJS* 36:595–619
- Draine BT, Anderson N. 1985. *ApJ* 292:494–499
- Draine BT, Aniano G, Krause O, Groves B, Sandstrom K, et al. 2014. *ApJ* 780:172
- Draine BT, Bond NA. 2004. *ApJ* 617:987–1003
- Draine BT, Dale DA, Bendo G, Gordon KD, Smith JDT, et al. 2007. *ApJ* 663:866–894
- Draine BT, Hensley B. 2012. *ApJ* 757:103
- Draine BT, Lazarian A. 1998. *ApJ* 494:L19+
- Draine BT, Li A. 2007. *ApJ* 657:810–837 (DL07)
- Duley WW, Williams DA. 1981. *MNRAS* 196:269–274
- Dumke M, Krause M, Wielebinski R. 2004. *A&A* 414:475–486
- Dwek E, Arendt RG, Bouchet P, Burrows DN, Challis P, et al. 2010. *ApJ* 722:425–434
- Dwek E, Scalo JM. 1980. *ApJ* 239:193–211
- Elias-Rosa N, Benetti S, Cappellaro E, Turatto M, Mazzali PA, et al. 2006. *MNRAS* 369:1880–1900
- Engelbracht CW, Gordon KD, Rieke GH, Werner MW, Dale DA, Latter WB. 2005. *ApJ* 628:L29–L32
- Evans PA, Willingale R, Osborne JP, O’Brien PT, Tanvir NR, et al. 2014. *MNRAS* 444:250–267
- Fendt C, Beck R, Neiningner N. 1998. *A&A* 335:123–133
- Finkelman I, Brosch N, Kniazev AY, Väisänen P, Buckley DAH, et al. 2010. *MNRAS* 409:727–736
- Fitzpatrick EL. 1999. *PASP* 111:63–75
- Fitzpatrick EL, Massa D. 2005. *AJ* 130:1127–1140
- Friis M, De Cia A, Krühler T, Fynbo JPU, Ledoux C, et al. 2015. *MNRAS* 451:167–183
- Fukui Y, Torii K, Onishi T, Yamamoto H, Okamoto R, et al. 2015. *ApJ* 798:6
- Galamez M, Hony S, Galliano F, Madden SC, Albrecht M, et al. 2013. *MNRAS* 431:1596–1617
- Galamez M, Kennicutt RC, Albrecht M, Aniano G, Armus L, et al. 2012. *MNRAS* 425:763–787
- Galamez M, Madden S, Galliano F, Hony S, Schuller F, et al. 2009. *A&A* 508:645–664
- Galliano F, A Dust SED Model with Hierarchical Bayesian Inference (I). *submitted*
- Galliano F, Dwek E, Charnial P. 2008. *ApJ* 672:214–243 (G08a)
- Galliano F, Hony S, Bernard JP, Bot C, Madden SC, et al. 2011. *A&A* 536:A88
- Galliano F, Madden SC, Jones AP, Wilson CD, Bernard JP. 2005. *A&A* 434:867–885
- Galliano F, Madden SC, Jones AP, Wilson CD, Bernard JP, Le Peintre F. 2003. *A&A* 407:159–176
- Galliano F, Madden SC, Tielens AGGM, Peeters E, Jones AP. 2008. *ApJ* 679:310–345 (G08b)
- Gao J, Jiang BW, Li A, Xue MY. 2013. *ApJ* 776:7
- Gillett FC, Forrest WJ, Merrill KM. 1973. *ApJ* 183:87–93
- Gordon KD, Clayton GC, Misselt KA, Landolt AU, Wolff MJ. 2003. *ApJ* 594:279–293 (G03)
- Gordon KD, Clayton GC, Witt AN, Misselt KA. 2000. *ApJ* 533:236–244
- Gordon KD, Engelbracht CW, Rieke GH, Misselt KA, Smith JDT, Kennicutt Jr. RC. 2008. *ApJ*

682:336–354

- Goudfrooij P, de Jong T. 1995. *A&A* 298:784
- Goudfrooij P, de Jong T, Hansen L, Norgaard-Nielsen HU. 1994. *MNRAS* 271:833
- Gould RJ, Salpeter EE. 1963. *ApJ* 138:393
- Greaves JS, Holland WS, Jenness T, Hawarden TG. 2000. *Nature* 404:732–733
- Guillet V, Fanciullo L, Verstraete L, Boulanger F, Jones AP, et al. 2017. *ArXiv e-prints*
- Guseva NG, Izotov YI, Fricke KJ, Henkel C. 2013. *A&A* 555:A90
- Haas M, Lemke D, Stickel M, Hippelein H, Kunkel M, et al. 1998. *A&A* 338:L33–L36
- Hall JS. 1949. *Science* 109:166–167
- Hao CN, Kennicutt RC, Johnson BD, Calzetti D, Dale DA, Moustakas J. 2011. *ApJ* 741:124
- Heckman TM, Lehnert MD. 2000. *ApJ* 537:690–696
- Heger ML. 1922. *Lick Observatory Bulletin* 10:141–145
- Helou G, Malhotra S, Hollenbach DJ, Dale DA, Contursi A. 2001. *ApJ* 548:L73–L76
- Hemachandra D, Barmby P, Peeters E, Willner SP, Ashby MLN, et al. 2015. *MNRAS* 454:818–830
- Hensley B, Murphy E, Staguhn J. 2015. *MNRAS* 449:809–819
- Hensley BS, Draine BT, Meisner AM. 2016. *ApJ* 827:45
- Herbig GH. 1995. *ARA&A* 33:19–74
- Hildebrand RH. 1983. *QJRAS* 24:267
- Hill RS, Cheng KP, Bohlin RC, O’Connell RW, Roberts MS, et al. 1995. *ApJ* 446:622
- Hiltner WA. 1949. *Science* 109:165
- Hinz JL, Engelbracht CW, Skibba R, Crocker A, Donovan Meyer J, et al. 2012. *ApJ* 756:75
- Hippelein H, Haas M, Tuffs RJ, Lemke D, Stickel M, et al. 2003. *A&A* 407:137–146
- Hirashita H. 2015. *MNRAS* 447:2937–2950
- Hobbs LM, York DG, Thorburn JA, Snow TP, Bishof M, et al. 2009. *ApJ* 705:32–45
- Hony S, Kemper F, Woods PM, van Loon JT, Gorjian V, et al. 2011. *A&A* 531:A137
- Hony S, Van Kerckhoven C, Peeters E, Tielens AGGM, Hudgins DM, Allamandola LJ. 2001. *A&A* 370:1030–1043
- Hopkins PF, Quataert E, Murray N. 2012. *MNRAS* 421:3522–3537
- Houck JR, Charmandaris V, Brandl BR, Weedman D, Herter T, et al. 2004. *ApJS* 154:211–214
- Huang X, Raha Z, Aldering G, Antilogus P, Bailey S, et al. 2017. *ApJ* 836:157
- Huchtmeier WK, Seiradakis JH, Materne J. 1981. *A&A* 102:134–141
- Hunt LK, Draine BT, Bianchi S, Gordon KD, Aniano G, et al. 2015. *A&A* 576:A33
- Hunt LK, Giovanardi C. 1992. *AJ* 104:1018–1038
- Hunt LK, Thuan TX, Izotov YI, Sauvage M. 2010. *ApJ* 712:164–187
- Hunter DA, Elmegreen BG, Martin E. 2006. *AJ* 132:801–818
- Hutton S, Ferreras I, Yershov V. 2015. *MNRAS* 452:1412–1420
- Imanishi M, Nakagawa T, Shirahata M, Ohyama Y, Onaka T. 2010. *ApJ* 721:1233–1261
- Israel FP. 1997. *A&A* 328:471–482
- Israel FP, Wall WF, Raban D, Reach WT, Bot C, et al. 2010. *A&A* 519:A67+
- Izotov YI, Stasińska G, Meynet G, Guseva NG, Thuan TX. 2006. *A&A* 448:955–970
- James BL, Aloisi A, Heckman T, Sohn ST, Wolfe MA. 2014. *ApJ* 795:109
- Jenkins EB. 2009. *ApJ* 700:1299–1348
- Jenkins EB, Wallerstein G. 2017. *ApJ* 838:85
- Jones AG, Bendo GJ, Baes M, Boquien M, Boselli A, et al. 2015. *MNRAS* 448:168–187
- Jones AP, Fanciullo L, Köhler M, Verstraete L, Guillet V, et al. 2013. *A&A* 558:A62
- Jones AP, Köhler M, Ysard N, Bocchio M, Verstraete L. 2017. *A&A* 602:A46 (J17)
- Jones AP, Tielens AGGM, Hollenbach DJ. 1996. *ApJ* 469:740
- Jones TJ. 2000. *AJ* 120:2920–2927
- Joseph RD, Meikle WPS, Robertson NA, Wright GS. 1984. *MNRAS* 209:111–122
- Jura M, Kim DW, Knapp GR, Guhathakurta P. 1987. *ApJ* 312:L11–L15
- Juvela M, Ysard N. 2012. *A&A* 539:A71

Kaneda H, Onaka T, Sakon I. 2007. *ApJ* 666:L21–L24

Kapala MJ, Groves B, Sandstrom K, Jarrett T, da Cunha E, et al. 2017. *ApJ* 842:128

Kawabata KS, Akitaya H, Yamanaka M, Itoh R, Maeda K, et al. 2014. *ApJ* 795:L4

Kelly BC, Shetty R, Stutz AM, Kauffmann J, Goodman AA, Launhardt R. 2012. *ApJ* 752:55

Kemper F, Vriend WJ, Tielens AGGM. 2004. *ApJ* 609:826–837

Kogut A, Banday AJ, Bennett CL, Gorski KM, Hinshaw G, et al. 1996. *ApJ* 464:L5

Köhler M, Ysard N, Jones AP. 2015. *A&A* 579:A15 (K15)

Kondo T, Kaneda H, Oyabu S, Ishihara D, Mori T, et al. 2012. *ApJ* 751:L18

Korn AJ, Keller SC, Kaufer A, Langer N, Przybilla N, et al. 2002. *A&A* 385:143–151

Lan TW, Ménard B, Zhu G. 2015. *MNRAS* 452:3629–3649

Lawton B, Churchill CW, York BA, Ellison SL, Snow TP, et al. 2008. *AJ* 136:994–1012

Le Petit F, Nehmé C, Le Bourlot J, Roueff E. 2006. *ApJS* 164:506–529

Lebouteiller V, Barry DJ, Spoon HWW, Bernard-Salas J, Sloan GC, et al. 2011. *ApJS* 196:8

Lebouteiller V, Heap S, Hubeny I, Kunth D. 2013. *A&A* 553:A16

Lebouteiller V, Péquignot D, Cormier D, Madden S, Pakull MW, et al. 2017. *A&A* 602:A45

Lee JC, Xiang J, Ravel B, Kortright J, Flanagan K. 2009. *ApJ* 702:970–979

Léger A, Puget JL. 1984. *A&A* 137:L5–L8

Leroy AK, Bolatto A, Gordon K, Sandstrom K, Gratier P, et al. 2011. *ApJ* 737:12

Li A, Greenberg JM. 2002. *ApJ* 577:789–794

Li Y, Calzetti D, Kennicutt RC, Hong S, Engelbracht CW, et al. 2010. *ApJ* 725:677–691

Lisenfeld U, Ferrara A. 1998. *ApJ* 496:145

Lisenfeld U, Israel FP, Stil JM, Sievers A. 2002. *A&A* 382:860–871

Lobo Gomes A, Magalhães AM, Pereyra A, Rodrigues CV. 2015. *ApJ* 806:94

Lonsdale Persson CJ, Helou G. 1987. *ApJ* 314:513–524

Lu N, Helou G, Werner MW, Dinerstein HL, Dale DA, et al. 2003. *ApJ* 588:199–217

Lutz D, Feuchtgruber H, Genzel R, Kunze D, Rigopoulou D, et al. 1996. *A&A* 315:L269–L272

Madden SC, Galliano F, Jones AP, Sauvage M. 2006. *A&A* 446:877–896

Madden SC, Poglitsch A, Geis N, Stacey GJ, Townes CH. 1997. *ApJ* 483:200–+

Maiolino R, Marconi A, Salvati M, Risaliti G, Severgnini P, et al. 2001. *A&A* 365:28–36

Malhotra S, Helou G, van Buren D, Kong M, Beichman CA, et al. 1996. *A&A* 315:L161–L164

Mallouris C. 2003. *ApJS* 147:265–303

Mason RE, Wright GS, Adamson A, Pendleton Y. 2007. *ApJ* 656:798–804

Matsuura M, Dwek E, Barlow MJ, Babler B, Baes M, et al. 2015. *ApJ* 800:50

Meijerink R, Tilanus RPJ, Dullemond CP, Israel FP, van der Werf PP. 2005. *A&A* 430:427–434

Melisse JPM, Israel FP. 1994. *A&A* 285:51–68

Mennella V, Brucato JR, Colangeli L, Palumbo P, Rotundi A, Bussoletti E. 1998. *ApJ* 496:1058

Mentuch E, Abraham RG, Zibetti S. 2010. *ApJ* 725:1971–1983

Mény C, Gromov V, Boudet N, Bernard JP, Paradis D, Nayral C. 2007. *A&A* 468:171–188

Micelotta ER, Jones AP, Tielens AGGM. 2010. *A&A* 510:A37

Montgomery JD, Clemens DP. 2014. *ApJ* 786:41

Mori TI, Sakon I, Onaka T, Kaneda H, Umehata H, Ohsawa R. 2012. *ApJ* 744:68

Muñoz-Mateos JC, Gil de Paz A, Boissier S, Zamorano J, Dale DA, et al. 2009a. *ApJ* 701:1965–1991

Muñoz-Mateos JC, Gil de Paz A, Zamorano J, Boissier S, Dale DA, et al. 2009b. *ApJ* 703:1569–1596

Murphy EJ, Helou G, Condon JJ, Schinnerer E, Turner JL, et al. 2010. *ApJ* 709:L108–L113

Nandy K, Morgan DH, Willis AJ, Wilson R, Gondhalekar PM. 1981. *MNRAS* 196:955–966

Oey MS. 1996. *ApJ* 467:666

Oliveira JM, van Loon JT, Sloan GC, Sewilo M, Kraemer KE, et al. 2013. *MNRAS* 428:3001–3033

Onaka T, Matsumoto H, Sakon I, Kaneda H. 2010. *A&A* 514:A15

Padoan P, Kim S, Goodman A, Staveley-Smith L. 2001. *ApJ* 555:L33–L36

Paradis D, Paladini R, Noriega-Crespo A, Mény C, Piacentini F, et al. 2012. *A&A* 537:A113

Paradis D, Reach WT, Bernard J, Block M, Engelbracht CW, et al. 2009. *AJ* 138:196–209

Patat F, Taubenberger S, Cox NLJ, Baade D, Clocchiatti A, et al. 2015. *A&A* 577:A53
 Peña-Guerrero MA, Peimbert A, Peimbert M, Ruiz MT. 2012. *ApJ* 746:115
 Peel MW, Dickinson C, Davies RD, Clements DL, Beswick RJ. 2011. *MNRAS* 416:L99–L103
 Peeters E, Martín-Hernández NL, Damour F, Cox P, Roelfsema PR, et al. 2002. *A&A* 381:571–605
 Peeters E, Spoon HWW, Tielens AGGM. 2004. *ApJ* 613:986–1003
 Perrin JM, Darbon S, Sivan JP. 1995. *A&A* 304:L21
 Phillips MM, Phillips AC, Heathcote SR, Blanco VM, Geisler D, et al. 1987. *PASP* 99:592–605
 Pierini D, Gordon KD, Witt AN, Madsen GJ. 2004. *ApJ* 617:1022–1046
 Pierini D, Majeed A, Boroson TA, Witt AN. 2002. *ApJ* 569:184–203
 Planck Collaboration, Abergel A, Ade PAR, Aghanim N, Alves MIR, et al. 2014. *A&A* 571:A11
 Planck Collaboration, Ade PAR, Aghanim N, Alina D, Alves MIR, et al. 2015a. *A&A* 576:A105
 Planck Collaboration, Ade PAR, Aghanim N, Alves MIR, Aniano G, et al. 2016. *A&A* 586:A132
 Planck Collaboration, Ade PAR, Aghanim N, Arnaud M, Ashdown M, et al. 2011a. *A&A* 536:A17
 Planck Collaboration, Ade PAR, Aghanim N, Arnaud M, Ashdown M, et al. 2011b. *A&A* 536:A20
 Planck Collaboration, Ade PAR, Aghanim N, Arnaud M, Ashdown M, et al. 2015b. *A&A* 582:A28
 Poglitsch A, Krabbe A, Madden SC, Nikola T, Geis N, et al. 1995. *ApJ* 454:293–+
 Popescu CC, Tuffs RJ. 2003. *A&A* 410:L21–L24
 Popescu CC, Tuffs RJ, Dopita MA, Fischera J, Kylafis ND, Madore BF. 2011. *A&A* 527:A109
 Reach WT, Boulanger F, Contursi A, Lequeux J. 2000. *A&A* 361:895–900
 Reach WT, Dwek E, Fixsen DJ, Hewagama T, Mather JC, et al. 1995. *ApJ* 451:188–+
 Reines AE, Johnson KE, Goss WM. 2008. *AJ* 135:2222–2239
 Reines AE, Johnson KE, Hunt LK. 2008. *AJ* 136:1415–1426
 Reines AE, Nidever DL, Whelan DG, Johnson KE. 2010. *ApJ* 708:26–37
 Rémy-Ruyer A, Madden SC, Galliano F, Galametz M, Takeuchi TT, et al. 2014. *A&A* 563:A31
 Rémy-Ruyer A, Madden SC, Galliano F, Hony S, Sauvage M, et al. 2013. *A&A* 557:A95
 Rémy-Ruyer A, Madden SC, Galliano F, Lebouteiller V, Baes M, et al. 2015. *A&A* 582:A121
 Ritchey AM, Wallerstein G. 2015. *PASP* 127:223
 Rodrigues CV, Magalhães AM, Coyne GV, Piirola SJV. 1997. *ApJ* 485:618–637
 Rodríguez-Ardila A, Contini M, Viegas SM. 2005. *MNRAS* 357:220–234
 Roman-Duval J, Bot C, Chasteney J, Gordon K. 2017. *ApJ* 841:72
 Roman-Duval J, Gordon KD, Meixner M, Bot C, Bolatto A, et al. 2014. *ApJ* 797:86
 Rosa MR, Benvenuti P. 1994. *A&A* 291:1–17
 Roth KC, Blades JC. 1997. *ApJ* 474:L95–L98
 Roussel H, Vigroux L, Bosma A, Sauvage M, Bonoli C, et al. 2001. *A&A* 369:473–509
 Rubin D, Hony S, Madden SC, Tielens AGGM, Meixner M, et al. 2009. *A&A* 494:647–661
 Sadler EM, Gerhard OE. 1985. *MNRAS* 214:177–187
 Sales DA, Pastoriza MG, Riffel R. 2010. *ApJ* 725:605–614
 Sandford SA, Bernstein MP, Materese CK. 2013. *ApJS* 205:8
 Sandstrom KM, Bolatto AD, Bot C, Draine BT, Ingalls JG, et al. 2012. *ApJ* 744:20
 Sandstrom KM, Bolatto AD, Draine BT, Bot C, Stanimirović S. 2010. *ApJ* 715:701–723
 Sauvage M, Blommaert J, Boulanger F, Cesarsky CJ, Cesarsky DA, et al. 1996. *A&A* 315:L89–L92
 Savage BD, Bohlin RC. 1979. *ApJ* 229:136–146
 Savage BD, Sembach KR. 1996. *ARA&A* 34:279–330
 Scaife AMM, Nikolic B, Green DA, Beck R, Davies ML, et al. 2010. *MNRAS* 406:L45–L49
 Scarrott SM, Foley NB, Gledhill TM, Wolstencroft RD. 1996. *MNRAS* 282:252–262
 Sellgren K. 1984. *ApJ* 277:623–633
 Sembach KR, Howk JC, Savage BD, Shull JM. 2001. *AJ* 121:992–1002
 Seok JY, Hirashita H, Asano RS. 2014. *MNRAS* 439:2186–2196
 Serkowski K, Mathewson DS, Ford VL. 1975. *ApJ* 196:261–290
 Shetty R, Kauffmann J, Schnee S, Goodman AA. 2009. *ApJ* 696:676–680
 Slavin JD, Dwek E, Jones AP. 2015. *ApJ* 803:7

- Smith BJ, Hancock M. 2009. *AJ* 138:130–145
- Smith JDT, Croxall K, Draine B, De Looze I, Sandstrom K, et al. 2017. *ApJ* 834:5
- Smith JDT, Draine BT, Dale DA, Moustakas J, Kennicutt RC, et al. 2007. *ApJ* 656:770–791 (S07)
- Smith MWL, Gomez HL, Eales SA, Ciesla L, Boselli A, et al. 2012. *ApJ* 748:123
- Smith RK, Valencic LA, Corrales L. 2016. *ApJ* 818:143
- Sofia UJ, Gordon KD, Clayton GC, Misselt K, Wolff MJ, et al. 2006. *ApJ* 636:753–764
- Sollerman J, Cox N, Mattila S, Ehrenfreund P, Kaper L, et al. 2005. *A&A* 429:559–567
- Spoon HWW, Tielens AGGM, Armus L, Sloan GC, Sargent B, et al. 2006. *ApJ* 638:759–765
- Stecher TP. 1965. *ApJ* 142:1683
- Stein W. 1966. *ApJ* 144:318
- Stepnik B, Abergel A, Bernard J, Boulanger F, Cambr esy L, et al. 2003. *A&A* 398:551–563
- Stevens JA, Amure M, Gear WK. 2005. *MNRAS* 357:361–380
- Stierwalt S, Armus L, Charmandaris V, Diaz-Santos T, Marshall J, et al. 2014. *ApJ* 790:124
- Tabatabaei FS, Braine J, Xilouris EM, Kramer C, Boquien M, et al. 2014. *A&A* 561:A95
- Tchernyshyov K, Meixner M, Seale J, Fox A, Friedman SD, et al. 2015. *ApJ* 811:78
- Tempel E, Tamm A, Tenjes P. 2010. *A&A* 509:A91
- Thorburn JA, Hobbs LM, McCall BJ, Oka T, Welty DE, et al. 2003. *ApJ* 584:339–356
- Thuan TX, Sauvage M, Madden S. 1999. *ApJ* 516:783–787
- Trehella M, Davies JI, Alton PB, Bianchi S, Madore BF. 2000. *ApJ* 543:153–160
- Tuffs RJ, Lemke D, Xu C, Davies JI, Gabriel C, et al. 1996. *A&A* 315:L149–L152
- van Loon JT, Bailey M, Tatton BL, Ma ız Apell aniz J, Crowther PA, et al. 2013. *A&A* 550:A108
- Vanzi L, Hunt LK, Thuan TX, Izotov YI. 2000. *A&A* 363:493–506
- Vega O, Bressan A, Panuzzo P, Rampazzo R, Clemens M, et al. 2010. *ApJ* 721:1090–1104
- Vermeij R, Peeters E, Tielens AGGM, van der Hulst JM. 2002. *A&A* 382:1042–1051
- Viaene S, Baes M, Tamm A, Tempel E, Bendo G, et al. 2017. *A&A* 599:A64
- Viaene S, De Geyter G, Baes M, Fritz J, Bendo GJ, et al. 2015. *A&A* 579:A103
- Vidal-Madjar A, Andreani P, Cristiani S, Ferlet R, Lanz T, Vladilo G. 1987. *A&A* 177:L17–L20
- Vogler A, Madden SC, Beck R, Lundgren AA, Sauvage M, et al. 2005. *A&A* 441:491–511
- Walsh W, Beck R, Thuma G, Weiss A, Wielebinski R, Dumke M. 2002. *A&A* 388:7–28
- Walter F, Cannon JM, Roussel H, Bendo GJ, Calzetti D, et al. 2007. *ApJ* 661:102–114
- Weingartner JC, Draine BT. 2001. *ApJS* 134:263–281
- Welty DE, Federman SR, Gredel R, Thorburn JA, Lambert DL. 2006. *ApJS* 165:138–172
- Welty DE, Lauroesch JT, Blades JC, Hobbs LM, York DG. 1997. *ApJ* 489:672–692
- Welty DE, Ritchey AM, Dahlstrom JA, York DG. 2014. *ApJ* 792:106
- Whelan DG, Lebouteiller V, Galliano F, Peeters E, Bernard-Salas J, et al. 2013. *ApJ* 771:16
- White III RE, Keel WC. 1992. *Nature* 359:129–131
- Witt AN, Vihj UP. 2004. *Extended Red Emission*. In *Astrophysics of Dust*, eds. AN Witt, GC Clayton, BT Draine, vol. 309 of *Astronomical Society of the Pacific Conference Series*
- Wood K, Whitney BA, Robitaille T, Draine BT. 2008. *ApJ* 688:1118–1123
- Wu R, Hogg DW, Moustakas J. 2011. *ApJ* 730:111
- Wu R, Madden SC, Galliano F, Wilson CD, Kamenetzky J, et al. 2015. *A&A* 575:A88
- Wu Y, Charmandaris V, Huang J, Spinoglio L, Tommasin S. 2009. *ApJ* 701:658–676
- Xilouris EM, Byun YI, Kylafis ND, Paleologou EV, Papamastorakis J. 1999. *A&A* 344:868–878
- Yamagishi M, Kaneda H, Ishihara D, Kondo T, Onaka T, et al. 2012. *A&A* 541:A10
- Yamagishi M, Kaneda H, Ishihara D, Oyabu S, Onaka T, et al. 2015. *ApJ* 807:29
- Yoshida M, Kawabata KS, Ohyama Y. 2011. *PASJ* 63:493–503
- Ysard N, K ohler M, Jones A, Miville-Desch enes MA, Abergel A, Fanciullo L. 2015. *A&A* 577:A110
- Zeegers ST, Costantini E, de Vries CP, Tielens AGGM, Chihara H, et al. 2017. *A&A* 599:A117
- Zhukovska S. 2014. *A&A* 562:A76
- Zubko V, Dwek E, Arendt RG. 2004. *ApJS* 152:211–249
- Zubko VG, Laor A. 2000. *ApJS* 128:245–269